

1 **Mechanistic investigations of the formation of multifunctional**  
2 **products from the multi-generation OH oxidation of styrene**

3 Long Chen,<sup>1,2,3</sup> Yu Huang,<sup>\*,1,2,3</sup> Yonggang Xue,<sup>1,2,3</sup> Long Cui,<sup>1,2,3</sup> Zhihui Jia<sup>4</sup>

4 <sup>1</sup> *State Key Laboratory of Loess Science, Institute of Earth Environment, Chinese*  
5 *Academy of Sciences, Xi'an 710061, China*

6 <sup>2</sup> *National Observation and Research Station of Regional Ecological Environment*  
7 *Change and Comprehensive Management in the Guanzhong Plain, Xi'an 710061,*  
8 *China*

9 <sup>3</sup> *Shaanxi Key Laboratory of Atmospheric and Haze-fog Pollution Prevention, Xi'an*  
10 *710061, China*

11 <sup>4</sup> *School of Materials Science and Engineering, Shaanxi Normal University, Xi'an,*  
12 *Shaanxi, 710119, China*

13

14

15

16

17 Submitted to *Atmospheric Chemistry & Physics*

18

19

20

21 \*Corresponding author:

22 Prof. Yu Huang, E-mail address: [huangyu@ieecas.cn](mailto:huangyu@ieecas.cn)

23

## 24 **Abstract**

25 Styrene is a highly reactive aromatic hydrocarbon that has been identified as a  
26 key secondary organic aerosol (SOA) precursor. Recent laboratory chamber  
27 experiments have identified C<sub>7</sub> and C<sub>8</sub> series compounds as the main components of  
28 SOA in the photooxidation of styrene. However, their molecular structures and  
29 formation pathways remain largely uncharacterized. Herein, the formation  
30 mechanisms of multifunctional products from the multi-generation OH oxidation of  
31 styrene are studied using the quantum chemistry methods. The calculations show that  
32 the first generation RO<sub>2</sub> radicals can either proceed unimolecular decomposition to  
33 yield benzaldehyde (C<sub>7</sub>H<sub>6</sub>O), or undergo bimolecular reactions with HO<sub>2</sub>/NO to form  
34 the first generation closed-shell C<sub>7</sub>- and C<sub>8</sub>-products, hydroperoxide 1<sup>st</sup>-ROOH  
35 (C<sub>8</sub>H<sub>10</sub>O<sub>3</sub>), benzaldehyde, and organic nitrate 1<sup>st</sup>-RONO<sub>2</sub> (C<sub>8</sub>H<sub>9</sub>NO<sub>3</sub>). For the second  
36 generation OH oxidation, OH-addition reaction occurring at the *ortho*-site of  
37 1<sup>st</sup>-ROOH and 1<sup>st</sup>-RONO<sub>2</sub> has a significant dominance. The *ortho*-OH-addition  
38 products can proceed through two O<sub>2</sub>-addition steps and a cyclization process to  
39 produce the peroxide bicyclic peroxy radicals (BPR). BPR can further react with  
40 HO<sub>2</sub>/NO to form the second generation closed-shell C<sub>8</sub>-products, hydroperoxide  
41 2<sup>nd</sup>-ROOH (C<sub>8</sub>H<sub>12</sub>O<sub>8</sub>), organic nitrate 2<sup>nd</sup>-RONO<sub>2</sub> (C<sub>8</sub>H<sub>10</sub>N<sub>2</sub>O<sub>10</sub>), and other  
42 multifunctional products, in which the first two products have fractional yields of 41.4%  
43 and 4.8%, respectively. For the third generation OH oxidation, OH-addition  
44 occurring at the C=C double bond of 2<sup>nd</sup>-ROOH and 2<sup>nd</sup>-RONO<sub>2</sub> has the lowest  
45 barrier. The major third generation closed-shell C<sub>8</sub>-products are the multifunctional  
46 hydroperoxides and organic nitrates. These findings carry important implications for  
47 advancing our understanding of the chemical composition and formation mechanisms  
48 of aromatic SOA.

49

## 50 **1. Introduction**

51 Aromatic compounds are recognized as the significant secondary organic aerosol  
52 (SOA) precursors, accounting for 20%-30% of the total volatile organic compounds

53 (VOCs) and up to ~60% of the urban atmosphere (Xu et al., 2020; Yan et al., 2019; Yu  
54 et al., 2022; Cabrera-Perez et al., 2016; Iyer et al., 2023; Wang et al., 2017; Bloss et  
55 al., 2005; Forstner et al., 1997). The primary sources include the incomplete  
56 combustion, solvent evaporation, and industrial emission, and the secondary sources  
57 involve the biofuel and biomass burning (Xu et al., 2020; Cabrera-Perez et al., 2016;  
58 Li et al., 2019). The most abundant aromatic compounds, including benzene, toluene,  
59 ethylbenzene, xylenes, styrene and trimethylbenzenes, are highly present in urban  
60 environments (Cabrera-Perez et al., 2016; Koppmann, 2008). The degradation of  
61 aromatic compounds initiated by the atmospheric oxidants (e.g., OH radicals, NO<sub>3</sub>  
62 radicals, O<sub>3</sub>, and Cl atom) leads to the production of multifunctional molecules (e.g.,  
63 nitroaromatics, dicarbonyls, cresols, epoxides) (Ji et al., 2017; Wu et al., 2014; Fu et  
64 al., 2023; Wang and Li, 2021; Wang et al., 2013; Zaytsev et al., 2019; Wang et al.,  
65 2020), significantly contributing to new particle formation (NPF) and SOA formation  
66 (up to 50% in eastern China) in the atmosphere (Wang et al., 2017; Wang et al., 2020;  
67 Garmash et al., 2020; Molteni et al., 2018; Nie et al., 2022).

68 The secondary organic aerosol formation potential (SOAP) of aromatics is  
69 significantly greater than that of alkanes and alkenes during haze episodes in Beijing  
70 (Sun et al., 2016). Among these precursors, toluene is the predominant SOA-forming  
71 species, contributing more than 16% of the total SOA, followed by styrene (15%) and  
72 ethylbenzene (9.5%) (Sun et al., 2016). Styrene is primarily emitted from the  
73 anthropogenic activities such as solvent usage and vehicle exhaust (Cho et al., 2014;  
74 Wu et al., 2021), which is detected at the ppb levels in urban environments, with the  
75 mixing ratios of 0.06-4.50 ppb (Cho et al., 2014; Huang et al., 2019). Styrene has  
76 been classified as a hazardous air pollutant in the 1990 Clean Air Act due to the  
77 potential mutagen and carcinogen (Environmental Protection Agency (EPA), 1990).  
78 Therefore, it is very necessary to investigate the degradation mechanisms of styrene  
79 under atmospheric conditions. In general, the atmospheric oxidation of styrene  
80 initiated by OH radicals is anticipated to be the dominant daytime sink, and the  
81 lifetime is estimated to be ~ 8 h under the conditions of typical OH radicals  
82 concentrations ( $[OH] = \sim 2 \times 10^6$  molecules cm<sup>-3</sup>) (Wu et al., 2021; Shen et al., 2022).

83 Due to the existence of highly reactive vinyl and aromatic groups, OH-initiated  
84 oxidation of styrene mainly comprise two kinds of pathways: H-abstraction and  
85 OH-addition, in which C<sub>β</sub>-site OH-addition reaction is expected to be the predominant  
86 pathway (Wu et al., 2021; Wang et al., 2015; Zhang et al., 2024). The formed products  
87 can combine with an O<sub>2</sub> molecule leading to the first generation peroxy radicals,  
88 which can further react with NO resulting in the formation of benzaldehyde and  
89 formaldehyde. The barrier of the rate-limiting step is predicted to be 28.4 kcal/mol  
90 (Wang et al., 2015), implying that benzaldehyde is unlikely to be the sole primary  
91 product in the oxidation of styrene due to their higher barriers. Additionally, carbonyl  
92 oxides, formed in the ozonolysis of styrene, serve as the chain units participating in  
93 the formation of oligomers (Yu et al., 2022). The volatility of oligomers decreases  
94 dramatically as the successive addition of carbonyl oxides increases, eventually  
95 transforming into extremely low volatility organic compounds (ELVOC) and directly  
96 participating in NPF.

97 Experimentally, Cho et al., investigated the kinetics of the reaction styrene  
98 + OH at 240-340 K and 1-3 Torr using the mass spectrometry technique (Cho et al.,  
99 2014). They found that the addition of OH radicals to the vinyl carbons is dominant,  
100 and the determined rate coefficient is  $(5.80 \pm 0.49) \times 10^{-11} \text{ cm}^3 \text{ molecule}^{-1} \text{ s}^{-1}$  at room  
101 temperature. In the smog chamber experiments, Tajuelo et al., (2019a, 2019b and  
102 2019c) found that the SOA yields from the photolysis and photooxidation of styrene  
103 and its homologous species increase with the concentration of initial reactants  
104 increasing, and benzaldehyde, benzoyl chloride, acetophenone and formaldehyde are  
105 expected to be the primary gas phase products. Yu et al. (2022) investigated the  
106 formation of SOA from styrene in an indoor chamber under different NO<sub>x</sub> and RH  
107 conditions, and found the SOA yields decrease with increasing RH in both the H<sub>2</sub>O<sub>2</sub>  
108 and NO<sub>x</sub> systems. The C<sub>7</sub> and C<sub>8</sub> species are the main products in the H<sub>2</sub>O<sub>2</sub> system,  
109 while organic nitrates are the major components in the NO<sub>x</sub> system. Although the  
110 possible molecular formula and chemical composition of the oxidation products from  
111 the reaction styrene + OH are given in the aforementioned studies, the specific  
112 molecular structures and formation pathways remain ambiguous. Additionally, to the

113 best of our knowledge, the majority of studies mainly focus on the first  
114 generation OH oxidation products to date, while the formation mechanisms of  
115 multifunctional products from the multi-generation OH oxidation of styrene are still  
116 limited.

117 In the present study, the multi-generation OH oxidation mechanisms of styrene  
118 in the presence of HO<sub>2</sub> /NO are investigated using the quantum chemistry methods.  
119 The calculated results arising from the first generation OH oxidation reactions are  
120 presented herein for comparison with the available literatures to ascertain the  
121 reliability of the employed theoretical method. For the multi-generation OH  
122 oxidation reactions of styrene, all the possible pathways, including H-abstraction,  
123 OH-addition, O<sub>2</sub>-addition, cyclization, ring-opening, intramolecular H-shifts, C-C  
124 bond and O-O bond scission, and HO<sub>2</sub>-elimination, are taken into account.  
125 Additionally, the saturated concentrations of the formed multifunctional products are  
126 estimated to identify the volatility classes.

## 127 **2. Computational methods**

### 128 **2.1 Electronic structures and energy calculations**

129 The electronic structures and energy calculations of all stationary points,  
130 including reactants (R), intermediates (IM), transition states (TS) and products (P), are  
131 performed using the Gaussian 16 program (Frisch et al., 2016). Geometric  
132 optimizations of all stationary points on the potential energy surfaces (PESs) are  
133 carried out at the M06-2X/6-31+g(d,p) level of theory, since it has reliable  
134 performance for describing the noncovalent interactions, thermochemical, and  
135 kinetics (Zhao and Truhlar, 2008). Harmonic vibrational frequencies are determined at  
136 the M06-2X/6-31+g(d,p) theoretical level to confirm the characteristics of all  
137 stationary points (a local minimum or a saddle point). The zero-point vibrational  
138 energy (ZPVE) is scaled by a factor of 0.967 (Alecú et al., 2010). Intrinsic reaction  
139 coordinate (IRC) calculations are carried out to ascertain the connection of the given  
140 TS between the designated local minima R and P (Fukui, 1981). Single point energy  
141 calculations are performed at the M06-2X/6-311++G(3df,3pd) level based on the

142 M06-2X/6-31+g(d,p) optimized geometries.

143 In order to further evaluate the reliability of the computational method employed  
144 herein, the single point energies of all the stationary points involved in the initial  
145 addition of OH radicals to styrene and intramolecular H-shift reactions of the first  
146 generation peroxy radicals S2-1-x are recalculated using the DLPNO-CCSD(T)/  
147 aug-cc-pVTZ method performed using the Orca 6.1 program (Neese, 2025). As shown  
148 in Table S1, the  $\Delta E_a$  values obtained using the M06-2X/6-311++G(3df,3pd) method  
149 are consistent with those derived from the DLPNO-CCSD(T)/aug-cc-pVTZ method.  
150 The largest deviation and the average absolute deviation are 1.2 and 0.6 kcal/mol,  
151 respectively, indicating that the computational method employed in this study is  
152 reliable. Considering the computational cost, the M06-2X/6-311++G(3df,3pd) method  
153 is employed to investigate the formation mechanism of multifunctional products from  
154 the multi-generation OH oxidation of styrene. The energy barrier ( $\Delta E_a$ ) and reaction  
155 energy ( $\Delta E_r$ ) are defined as the difference in energy between TS and IM, as well as  
156 between P and R.

## 157 **2.2 Conformer research**

158 RO<sub>2</sub> radicals formed from the addition of O<sub>2</sub> to the carbon-centered site of alkyl  
159 radicals R have multiple possible conformers due to the different orientations of O<sub>2</sub>  
160 attack (Chen et al., 2021; Fu et al., 2020; Møller et al., 2016 and 2020). An initial  
161 structure of RO<sub>2</sub> radicals is optimized at the B3LYP/6-31+G(d) level and  
162 subsequently used as the starting geometry to perform the conformer search  
163 conducted using the Molclus program (Lu, 2024). The resulting structures are initially  
164 optimized at the B3LYP/6-31+G(d) level, as this method accurately predicts the  
165 relative energy ordering of different conformers (Møller et al., 2016 and 2020). For  
166 the intramolecular H-shift reactions of RO<sub>2</sub> radicals, the lengths of the O-O, C-H and  
167 O-H bonds in the conformational sampling of TSs are constrained to retain the cyclic  
168 TS structure. All unique conformers of R, TS and P within 5.0 kcal/mol with respect  
169 to the lowest energy conformer are further optimized at the M06-2X/6-31+g(d,p) level  
170 of theory. Then, the single point energy calculations are performed at the

171 M06-2X/6-311++G(3df,3pd) level of theory. RO radicals formed by the bimolecular  
172 reactions of RO<sub>2</sub> radicals with HO<sub>2</sub> radicals and NO also have multiple conformers. In  
173 order to obtain the lowest energy conformer, a similar methodology is employed in  
174 the present study.

## 175 **2.3 Kinetics calculations**

176 The rate coefficients of unimolecular reactions, including intramolecular H-shifts,  
177 cyclization, HO<sub>2</sub>-elimination, and C-C bond and C-O bond scissions, are calculated  
178 using the RRKM theory along with energy-grained master equation (RRKM-ME)  
179 (Holbrook et al., 1996). The rate coefficients of bimolecular reactions, involving  
180 H-abstraction and OH-addition, are determined using the traditional transition state  
181 theory (TST) (Fernández-Ramos et al., 2007). An asymmetric one-dimensional Eckart  
182 model (Eckart, 1930) is employed to consider the tunneling correction factors in the  
183 rate coefficient calculations based on RRKM-ME and TST. A single exponential down  
184 model in the RRKM-ME calculations is utilized to approximate the collision transfer  
185 ( $\langle \Delta E \rangle_{\text{down}} = 200 \text{ cm}^{-1}$ ). The Lennard-Jones parameters of all intermediate species are  
186 estimated using the empirical formula as proposed by Gilbert and Smith (1990).

187 For the intramolecular H-shifts of RO<sub>2</sub> and RO radicals, the rate coefficients are  
188 computed using the multiconformer transition state theory (MC-TST) (Møller et al.,  
189 2016), which is expressed as Eq. (1): (Møller et al., 2016 and 2020; Pasik et al., 2024)

$$190 \quad k_{\text{MC-TST}} = \kappa \frac{k_{\text{B}}T}{h} \frac{\sum_i^{\text{TS conf.}} \exp\left(\frac{-\Delta E_i}{k_{\text{B}}T}\right) Q_{\text{TS},i}}{\sum_j^{\text{R conf.}} \exp\left(\frac{-\Delta E_j}{k_{\text{B}}T}\right) Q_{\text{R},j}} \exp\left(-\frac{E_{\text{TS}} - E_{\text{R}}}{k_{\text{B}}T}\right) \quad (1)$$

191 where  $\kappa$  is the Eckart tunneling coefficient,  $h$  is Planck's constant,  $k_{\text{B}}$  is  
192 Boltzmann's constant, and  $T$  is the absolute temperature (298.15 K).  $Q_{\text{TS},i}$  and  $Q_{\text{R},j}$   
193 refer to the partition functions of the corresponding transition state  $i$  and reactant  $j$   
194 conformers, respectively.  $\Delta E_i$  and  $\Delta E_j$  represent the relative electronic energies  
195 between the corresponding transition state  $i$  and reactant  $j$  conformers and the lowest  
196 energy conformers, respectively.  $E_{\text{TS}}$  and  $E_{\text{R}}$  stand for the electronic energies of the  
197 lowest energy transition state and reactant conformers, respectively. All kinetics  
198 calculations are carried out using the KiSThelP 2021 and MESMER 6.0 programs

199 (Glowacki et al., 2012; Canneaux et al., 2013).

## 200 **3. Results and discussion**

### 201 **3.1 First generation OH oxidation mechanisms of styrene**

202 Styrene is composed of a benzene ring and a vinyl group, and its oxidation  
203 initiated by OH radicals may proceed either on the vinyl group or on the benzene ring.  
204 Previous literature has demonstrated that the addition of OH radicals to terminal  
205 carbon ( $C_{\beta}$ -site) of a vinyl group in styrene is the dominant pathway, with the  
206 branching ratio of 88.2% (Wu et al., 2021). Therefore, the  $C_{\beta}$ -site OH-addition  
207 reaction is mainly considered in the present study. Figure 1 depicts that this reaction  
208 starts with the formation of a pre-reactive complex IM1, and then transforms into an  
209 alkyl radical S1-1 via transition state TS1 with a  $\Delta E_a$  of 0.8 kcal/mol. The rate  
210 coefficient of  $C_{\beta}$ -site OH-addition reaction is estimated to be  $1.5 \times 10^{-11} \text{ cm}^3$   
211  $\text{molecule}^{-1} \text{ s}^{-1}$  at ambient temperature, which is approximately consistent with the  
212 experimental ( $1.2\text{-}6.2 \times 10^{-11} \text{ cm}^3 \text{ molecule}^{-1} \text{ s}^{-1}$ ) and theoretical values ( $1.7\text{-}2.0 \times$   
213  $10^{-11} \text{ cm}^3 \text{ molecule}^{-1} \text{ s}^{-1}$ ) for the total rate coefficient of the reaction styrene + OH  
214 (Wu et al., 2021; Zhang et al., 2024).

215 Due to the existence of resonance structures with radical character on the  
216 aromatic ring, the resulting S1-1 can readily isomerize into three other species,  
217 namely, S1-2, S1-3 and S1-4. The attack of an  $\text{O}_2$  molecule on the C-center site of  
218 S1-1 leads to the formation of the first generation peroxy radicals S2-1-x ( $\Delta E_r > -59.6$   
219 kcal/mol). The formed S2-1-x includes eight energetically similar conformers due to  
220 the different orientations of  $\text{O}_2$  attack. In order to distinguish the different conformers,  
221 the subscript letter x is used in the present study. The energy ordering of different  
222 conformers follows an alphabetical sequence, in which letter a denotes the lowest  
223 energy conformer. The Boltzmann population of different conformers in S2-1-x is  
224 listed in Table S2.

225 For the unimolecular decomposition reactions of S2-1-x, there are three kinds of  
226 pathways. One is the intramolecular H-shift reactions, where the hydrogen atom  
227 migrates from the  $-\text{CH}_2$ ,  $-\text{CH}$  and  $-\text{OH}$  groups to the terminal oxygen atom of the –

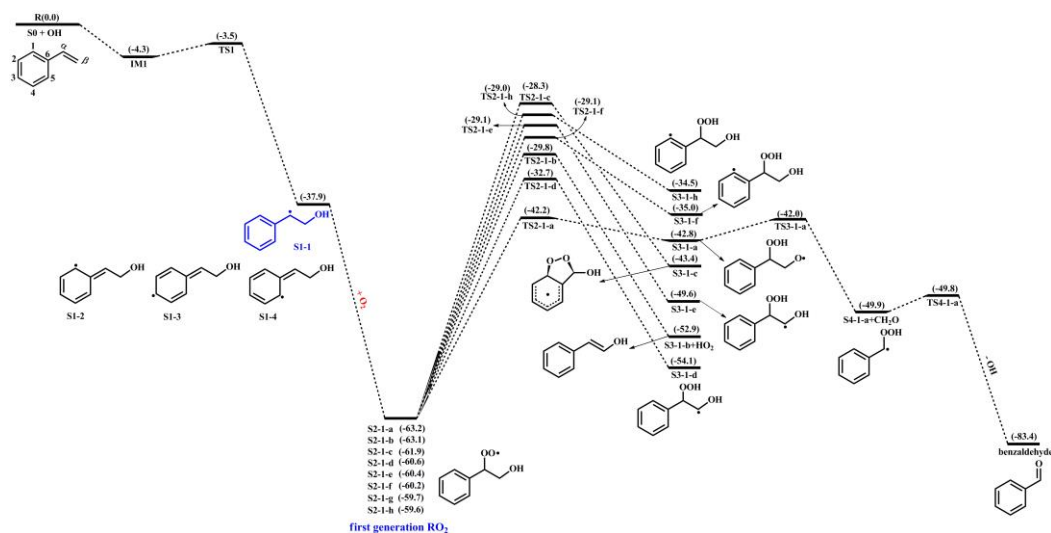
228 OO group leading to various alkyl and alkoxy radicals. Among these competing  
229 H-shift reactions, the hydrogen atom at the –OH group can be transferred via a  
230 six-membered ring transition state (1,5-H shift) to yield an alkoxy radical S3-1-a,  
231 which exhibits the lowest barrier ( $\Delta E_a = 21.0$  kcal/mol). The resulting S3-1-a can  
232 undergo the  $C_\alpha$ - $C_\beta$  bond cleavage to produce a formaldehyde and an alkyl radical  
233 S4-1-a ( $\Delta E_a = 0.8$  kcal/mol), followed by an OH radical release to form benzaldehyde  
234 ( $\Delta E_a = 0.1$  kcal/mol). The rate coefficients for the aforementioned three pathways are  
235 calculated to be  $2.7 \times 10^{-4}$ ,  $4.6 \times 10^{10}$  and  $7.2 \times 10^{10} \text{ s}^{-1}$ , respectively. Based on the  
236 values of  $\Delta E_a$  and the corresponding rate coefficients, it can be concluded that the  
237 1,5-H shift reaction is the rate-determining step in the formation of benzaldehyde. The  
238 other is the cyclization, where the –OO group attacks the C=C double bond in the  
239 benzene ring forming a cyclic peroxide alkyl radical S3-1-c ( $\Delta E_a = 33.6$  kcal/mol).  
240 The last is the HO<sub>2</sub>-elimination, where a concerted process of  $C_\alpha$ -O and  $C_\beta$ -H bonds  
241 scission forms a closed-shell species S3-1-b and a HO<sub>2</sub> radical byproduct ( $\Delta E_a = 33.3$   
242 kcal/mol). The aforementioned results show that the cyclization and HO<sub>2</sub>-elimination  
243 reactions are less important due to their higher barriers.

244 As depicted in Figure S1, the formations of the first generation peroxy radicals  
245 S2-2-x from the association reaction S1-2 + O<sub>2</sub> are strongly endothermic ( $\Delta E_r =$   
246 8.1-10.4 kcal/mol), suggesting that they have a significant potential to redissociate  
247 back to reactants S1-2 and O<sub>2</sub>. The resulting S2-2-x can undergo through various  
248 intramolecular H-shifts to yield distinct C-centered and O-centered radicals. Among  
249 these competing H-shift pathways, hydrogen transfer from the –OH group to the  
250 terminal oxygen of –OO group has the lowest barrier ( $\Delta E_a = 17.4$  kcal/mol). A similar  
251 conclusion is also obtained from the association reactions S1-3 + O<sub>2</sub> ( $\Delta E_r = 6.6$ -7.1  
252 kcal/mol) and S1-4 + O<sub>2</sub> ( $\Delta E_r = 8.1$ -11.1 kcal/mol) that the formations of the first  
253 generation peroxy radicals S2-3-x and S2-4-x are thermochemically unfavorable, and  
254 their subsequent intramolecular H-shift barriers are considerably high (Figures S2 and  
255 S3). Therefore, in the present study, we mainly focus on the subsequent reaction  
256 mechanisms of S2-1-x under both low and high NO<sub>x</sub> conditions.

257 In the low-NO<sub>x</sub> conditions, the bimolecular reaction with HO<sub>2</sub> radicals is  
258 expected to be the dominant sink for RO<sub>2</sub> radicals (Orlando and Tyndall, 2012;  
259 Vereecken et al., 2015). Previous studies have reported that the rate coefficient  
260  $k_{\text{RO}_2+\text{HO}_2}$  for the reactions of alkyl peroxy radicals with HO<sub>2</sub> radicals is  $1.7 \times 10^{-11}$   
261  $\text{cm}^3 \text{ molecule}^{-1} \text{ s}^{-1}$  (Atkinson and Arey, 2003; Boyd et al., 2003). The typical  
262 atmospheric concentration of HO<sub>2</sub> radicals is 20-40 pptv (Wang et al., 2017; Bianchi  
263 et al., 2019), resulting in the pseudo-first-order rate constant  $k'_{\text{RO}_2+\text{HO}_2} = k_{\text{RO}_2+\text{HO}_2}$   
264  $[\text{HO}_2]$  of 0.01-0.02  $\text{s}^{-1}$ . The isomerization reaction of RO<sub>2</sub> radicals is competitive with  
265 the bimolecular reactions with HO<sub>2</sub> radicals only when the rate coefficient of  
266 intramolecular H-shifts exceeds 0.01-0.02  $\text{s}^{-1}$ . In the high-NO<sub>x</sub> conditions, the  
267 bimolecular reaction of RO<sub>2</sub> radicals with NO is considered to be a dominant sink  
268 (Orlando and Tyndall, 2012; Vereecken et al., 2015). The rate coefficient  $k_{\text{RO}_2+\text{NO}}$  for  
269 the reaction of alkyl peroxy radicals with NO is determined to be  $9.0 \times 10^{-12} \text{ cm}^3$   
270  $\text{molecule}^{-1} \text{ s}^{-1}$  (Atkinson and Arey, 2003; Bianchi et al., 2019). The typical  
271 atmospheric concentration of NO is 0.4-40 ppbv (Wang et al., 2017; Bianchi et al.,  
272 2019), leading to the pseudo-first-order rate constant  $k'_{\text{RO}_2+\text{NO}} = k_{\text{RO}_2+\text{NO}} [\text{NO}]$  of  
273 0.1-10  $\text{s}^{-1}$ . The intramolecular H-shift reaction of RO<sub>2</sub> radicals can compete with the  
274 bimolecular reaction with NO only when the rate coefficient of the former case  
275 exceeds 10  $\text{s}^{-1}$ . Therefore, we use the  $k'_{\text{RO}_2+\text{HO}_2}$  (0.01-0.02  $\text{s}^{-1}$ ) and  $k'_{\text{RO}_2+\text{NO}}$  (0.1-10  $\text{s}^{-1}$ )  
276 values as thresholds to evaluate the relative importance of the isomerization reactions  
277 of RO<sub>2</sub> radicals under both low- and high-NO<sub>x</sub> conditions. Previous studies have also  
278 employed the same methodology to evaluate the relative importance of isomerization  
279 and bimolecular reactions of RO<sub>2</sub> radicals during the OH-initiated oxidation of  
280 organophosphate esters and alkylbenzenes (Wang et al., 2017; Fu et al., 2024). For the  
281 intramolecular H-shift reactions of S2-1-x, the rate coefficient  $k_{\text{MC-TST}}$  is estimated to  
282 be  $1.6 \times 10^{-4} \text{ s}^{-1}$ , which is 2-4 orders of magnitude lower than  $k'_{\text{RO}_2+\text{HO}_2}$  and  $k'_{\text{RO}_2+\text{NO}}$ ,  
283 indicating that the isomerization reaction of S2-1-x is less competitive than the  
284 bimolecular reactions with HO<sub>2</sub> radicals and NO.

285 In the presence of NO, the bimolecular reactions of S2-1-x with NO initially  
286 proceed via oxygen-to-oxygen coupling to yield organic nitrites ROONO, which

287 subsequently decompose into benzaldehyde and  $\text{CH}_2\text{OH}$  radical or isomerize to  
 288 organic nitrates  $\text{RONO}_2$ . The energy barrier of the rate-limiting step predicted in  
 289 Wang's study for the formation of benzaldehyde is 28.4 kcal/mol, which is  
 290 approximately 4.0 kcal/mol greater than that for the formation of  $\text{RONO}_2$  (Wang et al.,  
 291 2015). In the absence of  $\text{NO}$ , the hydroperoxides  $\text{ROOH}$  formed from the bimolecular  
 292 reaction of  $\text{S2-1-x}$  with  $\text{HO}_2$  radicals are anticipated to be the dominate products. The  
 293 aforementioned results are further confirmed by the recent smog chamber experiment  
 294 study that  $\text{C}_7$  and  $\text{C}_8$  series products, as well as organic nitrates are the main  
 295 components of SOA in the  $\text{OH}$ -initiated oxidation of styrene under different  $\text{NO}_x$   
 296 conditions (Yu et al., 2022). Considering that the extensive studies on the  $\text{OH}$ -initiated  
 297 oxidation of benzaldehyde have done (Sebbar et al., 2011; Zhao et al., 2022; Iuga et  
 298 al., 2008), this study primarily focuses on the multi-generation  $\text{OH}$  oxidation  
 299 mechanisms of  $\text{ROOH}$  and  $\text{RONO}_2$  under both low- and high- $\text{NO}_x$  conditions.



300

301 **Figure 1.** PES for the first-stage oxidation of styrene initiated by  $\text{OH}$  radicals and the  
 302 isomerization reactions of  $\text{S2-1-x}$  at the  $\text{M06-2X/6-311++G(3df,3pd)}/\text{M06-2X/6-31+g(d,p)}$  level

### 303 3.2 Second generation $\text{OH}$ oxidation mechanisms of $1^{\text{st}}\text{-ROOH}$ 304 and $1^{\text{st}}\text{-RONO}_2$

305 The first generation products, including hydroperoxides  $1^{\text{st}}\text{-ROOH}$  and organic  
 306 nitrates  $1^{\text{st}}\text{-RONO}_2$ , include multiple conformers. To obtain the global minimum of  
 307  $1^{\text{st}}\text{-ROOH}$  and  $1^{\text{st}}\text{-RONO}_2$ , the conformer search is performed by using the Molclus  
 308 program. The resulting structures are initially optimized at the  $\text{M06-2X/6-31+g(d,p)}$

309 level, then the single point energies are calculated at the M06-2X/6-311++G(3df,3pd)  
310 level. The global minimum structures of 1<sup>st</sup>-ROOH (S4) and 1<sup>st</sup>-RONO<sub>2</sub> (S5) are  
311 presented in Figure S4.

### 312 **3.2.1 The oxidation mechanism of 1<sup>st</sup>-ROOH initiated by OH** 313 **radicals**

314 The reaction 1<sup>st</sup>-ROOH (S4) + OH proceeds through the addition of OH radicals  
315 to either side of the benzene ring to yield various alkyl radicals, as depicted in Figure  
316 2. In the present study, *syn*-OH-addition is defined as the scenario in which the  
317 addition of OH radicals occurs at the same side as the –OOH group, while  
318 *anti*-OH-addition is referred to the scenario in which the addition of OH radicals  
319 occurs at the opposite side as the –OOH group. For the *syn*-OH-addition reactions, the  
320 addition of OH radicals to the C1-site of 1<sup>st</sup>-ROOH (S4) exhibits the lowest barrier  
321 ( $\Delta E_a = 3.6$  kcal/mol) due to the stability of the formed product, P<sub>S4-add1</sub>'. A similar  
322 conclusion is also obtained from the *anti*-OH-addition reactions that the OH-addition  
323 pathway occurring at the C1-site is favorable ( $\Delta E_a = 0.8$  kcal/mol). Notably, the  
324 preferred OH-addition pathway in the *anti*-OH-addition reactions exhibits greater  
325 competitiveness compared to that in the *syn*-OH-addition reactions. It can be  
326 explained by the greater steric hindrance present in the latter reaction. In order to  
327 further evaluate the reliability of our results,  $\Delta E_a$  of all the *syn*-OH-addition and  
328 *anti*-OH-addition reactions are recalculated using the DLPNO-CCSD(T)/  
329 aug-cc-pVTZ//M06-2X/6-311+G(d,p) method. As shown in Table S3, the  $\Delta E_a$  values  
330 obtained using the M06-2X/6-311++G(3df,3pd) method are in good agreement with  
331 those derived from the DLPNO-CCSD(T)/aug-cc-pVTZ method. The largest  
332 deviation and the average absolute deviation are 1.2 and 0.9 kcal/mol, respectively,  
333 indicating that the M06-2X/6-311++G(3df,3pd) method employed in this study is  
334 reliable. Based on the values of  $\Delta E_a$  obtained using the DLPNO-CCSD(T)/  
335 aug-cc-pVTZ method, it can also be concluded that the addition of OH radicals to  
336 C1-site, occurring at the opposite direction relative to the –OOH group, is  
337 energetically favorable. The rate coefficients of the addition of OH radicals to the

338 different sites of 1<sup>st</sup>-ROOH are calculated to be  $8.2 \times 10^{-12}$  (C1-site),  $5.8 \times 10^{-15}$   
339 (C2-site),  $8.3 \times 10^{-15}$  (C3-site),  $8.6 \times 10^{-15}$  (C4-site),  $2.7 \times 10^{-12}$  (C5-site) and  $4.1 \times$   
340  $10^{-13}$  (C6-site)  $\text{cm}^3 \text{ molecule}^{-1} \text{ s}^{-1}$ , respectively. The branching ratios for OH addition  
341 to the C1, C5 and C6 sites are predicted to be 72.4%, 23.8% and 3.6%, respectively,  
342 while the sum of branching ratios for OH addition to other carbon sites is less than  
343 1%.

344 Our result is opposite to Zhang's finding that the addition of OH radicals to  
345 C6-site would be the most favorable pathway (Zhang et al., 2024). The discrepancy  
346 can be explained by the following three factors: (1) The 1<sup>st</sup>-ROOH conformer selected  
347 in the Zhang's study is not the global minimum. In the present study, the global  
348 minimum conformer of 1<sup>st</sup>-ROOH, identified through the conformer search, is found  
349 to be 2.2 kcal/mol lower than the 1<sup>st</sup>-ROOH structure selected in the Zhang's study. (2)  
350 The pre-reactive complexes are not considered in the Zhang's study. The addition of  
351 OH radicals to C1-, C2-, C3- and C6-sites, occurring at the opposite direction relative  
352 to the -OOH group, are merely considered in the Zhang's study. They found that the  
353 apparent energy barrier of the addition of OH radicals to C6-site is smallest, and is  
354 therefore expected to be the favorable pathway. Actually, these OH-addition reactions  
355 are modulated by the pre-reactive complexes. It may be inappropriate to determine the  
356 favorable pathway based solely on apparent activation energy without considering the  
357 pre-reaction complexes. (3) From a geometric perspective, the addition of OH radicals  
358 to C6-site is associated with greater steric hindrance compared to other sites, as  
359 C6-atom connects with a larger functional group. Base on the aforementioned  
360 discussions, we believe that the addition of OH radicals to C6-site is unlikely to be the  
361 dominant pathway. Our calculations also confirm that the addition of OH radicals to  
362 C6-site is less importance compared to that at the C1-site.

363 Our conclusion is further supported by the reaction toluene + OH that the  
364 *ortho*-OH-addition reaction exhibits significant dominance, with the branching ratio  
365 of up to 69.8-75.8% (Ji et al., 2017; Zhang 2019; Wu et al., 2020). Considering the  
366 high reactivity of *ortho*-OH-addition in the reactions toluene + OH and 1<sup>st</sup>-ROOH  
367 (S4) + OH, the substitute effects of the -CH<sub>3</sub> and -OOH groups are explicitly

368 discussed in the present study. Notably, the  $-\text{CH}_3$  group in toluene is bonded to the C6  
369 atom, and the  $-\text{OOH}$  group in 1<sup>st</sup>-ROOH is bonded to the C $\alpha$  atom, as depicted in  
370 Figure S5. The optimized geometries of toluene and 1<sup>st</sup>-ROOH and the NPA atomic  
371 charges of all the carbon atoms in the benzene ring are displayed in Figure S5. The  
372 C-C bond lengths and the C-C-C bond angles in the benzene ring of toluene are  
373 approximately 1.39 Å and 120°, respectively, which are consistent with those in the  
374 benzene ring of 1<sup>st</sup>-ROOH. The aforementioned results show the effect of the  $-\text{CH}_3$   
375 and  $-\text{OOH}$  groups on the geometric structure of benzene ring is negligible. From the  
376 perspective of NPA atomic charges, the charges on the C1 (-0.246 e) and C5 (-0.246 e)  
377 atoms are more greater than those on the other carbon atoms in the benzene ring of  
378 toluene. And the OH-adduct formed from the *ortho*-OH-addition reaction exhibits the  
379 greater stability. These results indicate that the  $-\text{CH}_3$  group is a typical *ortho*-directing  
380 substituent and exerts an activating effect on the *ortho*-site of the benzene ring, which  
381 explains why the *ortho*-OH-addition reaction is predominant in the reaction toluene  
382 + OH. Compared with the charges on the carbon atoms in the benzene ring of toluene,  
383 the charges on C1 and C6 atoms increase by 0.013 e and 0.057 e, respectively, in  
384 1<sup>st</sup>-ROOH, which can be attributed to the electron-withdrawing effect of the  $-\text{OOH}$   
385 group. The charge on the C1 atom (-0.259 e) is the highest, and the stability of the  
386 resulting OH-adduct is the greatest, implying that the addition of OH radicals to  
387 C1-site is dominant in the reaction 1<sup>st</sup>-ROOH + OH. Therefore, a direct comparison  
388 of the favorable OH-addition pathway in the reactions toluene + OH and 1<sup>st</sup>-ROOH  
389 (S4) + OH is performed in this study.

390 The formed product P<sub>S4-add1</sub> includes two conjugate double bonds (C<sub>2</sub>=C<sub>3</sub> and  
391 C<sub>4</sub>=C<sub>5</sub>), which can readily isomerize to P<sub>S4-add2</sub> and P<sub>S4-add3</sub>, as evident from Figure S6.  
392 In the present of O<sub>2</sub>, the attack of an O<sub>2</sub> molecule on the C-centered site of P<sub>S4-add1</sub>,  
393 P<sub>S4-add2</sub>, and P<sub>S4-add3</sub> proceed via the barrierless processes to produce the second  
394 generation peroxy radicals P<sub>S4-add1-a/-s</sub>, P<sub>S4-add2-a/-s</sub> and P<sub>S4-add3-a/-s</sub>. The O<sub>2</sub>-addition  
395 reaction occurring at the same direction as the  $-\text{OOH}$  group is defined as  
396 *syn*-O<sub>2</sub>-addition, while the O<sub>2</sub>-addition reaction occurring at the opposite direction as  
397 the  $-\text{OOH}$  group is defined as *anti*-O<sub>2</sub>-addition. For the reaction P<sub>S4-add1</sub> + O<sub>2</sub> →

398  $P_{S4-add1-a/-s}$ ,  $\Delta E_r$  of *anti*-O<sub>2</sub>-addition is -5.8 kcal/mol, which is lower than that of  
399 *syn*-O<sub>2</sub>-addition by 0.4 kcal/mol, suggesting that *anti*-O<sub>2</sub>-addition is preferable over  
400 *syn*-O<sub>2</sub>-addition in energy. For the reactions  $P_{S4-add2} + O_2 \rightarrow P_{S4-add2-a/-s}$  and  $P_{S4-add3} +$   
401  $O_2 \rightarrow P_{S4-add3-a/-s}$ , it can be concluded the same by the  $\Delta E_r$  values that  
402 *anti*-O<sub>2</sub>-addition reaction is energetically feasible.

403 The resulting  $P_{S4-add1-a/-s}$  can proceed intramolecular cyclization reaction, where  
404 the attack of end-site oxygen atom of the -OO group on C2-site of the C<sub>2</sub>=C<sub>3</sub> double  
405 bond, leading to the formation of peroxide bicyclic alkyl radicals.  $\Delta E_a$  and  $\Delta E_r$  of the  
406 reaction  $P_{S4-add1-a} \rightarrow P_{S4-add1-a-1}$  are 11.8 and -16.8 kcal/mol, respectively, which are  
407 lower than those of the reaction  $P_{S4-add1-s} \rightarrow P_{S4-add1-s-1}$  by 3.9 and 2.2 kcal/mol,  
408 respectively. The aforementioned results reveal that the intramolecular cyclization  
409 reaction of *anti*-O<sub>2</sub>-addition product  $P_{S4-add1-a}$  is favorable on both thermochemically  
410 and kinetically. A similar conclusion is also derived from the intramolecular  
411 cyclization reactions of *anti*-O<sub>2</sub>-addition products  $P_{S4-add2-a}$  and  $P_{S4-add3-a}$ . Notably, the  
412 barriers of the intramolecular cyclization reactions  $P_{S4-add2-a} \rightarrow P_{S4-add2-a-1}$  ( $\Delta E_a =$   
413 31.1 kcal/mol) and  $P_{S4-add2-a} \rightarrow P_{S4-add2-a-2}$  ( $\Delta E_a = 34.6$  kcal/mol) are extremely high,  
414 making them insignificant in the atmosphere. The tautomerization between  
415  $P_{S4-add1-a-1}$  and  $P_{S4-add3-a-1}$  readily occurs due to the existence of resonance structures,  
416 and it is therefore that the latter conformer is selected as a prototype for the  
417 investigating of its subsequent reaction mechanism.

418 The formed  $P_{S4-add3-a-1}$  can combine with an O<sub>2</sub> molecule leading to the third  
419 generation peroxy radicals (also called as peroxide bicyclic peroxy radicals, BPR)  
420  $P_{S4-add3-a-2}$ , and the lowest energy conformer is presented in Figure S7. The  
421 isomerization of  $P_{S4-add3-a-2}$  may undergo through a concerted process of the cleavage  
422 of -O-O- bridge bond and C<sub>1</sub>-C<sub>2</sub> bond as well as hydrogen atom transfer from the  
423 hydroxyl group to the bridge oxygen atom, yielding a new peroxy radical ( $\Delta E_a = 28.5$   
424 kcal/mol). The room temperature rate coefficient is calculated to be  $3.0 \times 10^{-9} \text{ s}^{-1}$ ,  
425 which is several orders of magnitude low than the typical pseudo-first-order rate  
426 constants  $k'_{RO_2+HO_2}$  (0.01-0.02 s<sup>-1</sup>) and  $k'_{RO_2+NO}$  (0.1-10 s<sup>-1</sup>), suggesting that the  
427 isomerization reaction is less importance in the atmosphere. Therefore, the

428 bimolecular reactions of  $P_{S4-add3-a-2}$  with  $HO_2$  radicals with NO are mainly taken into  
429 consideration in this study.

430 In the pristine environments,  $P_{S4-add3-a-2}$  can react with  $HO_2$  radicals resulting in  
431 the formation of the second generation products, bicyclic hydroperoxide 2<sup>nd</sup>-ROOH  
432 (S6) and peroxide bicyclic alkoxy radical (BAR)  $P_{S4-add3-a-3}$ , as depicted in Figure S7.  
433 For the subsequent reactions of S6 initiated by OH radicals, the detailed mechanisms  
434 are discussed in Section 3.3.1. From Figure 3, it can be seen that the unimolecular  
435 decomposition of  $P_{S4-add3-a-3}$  involves two kinds of pathways. One is the ring-opening  
436 reaction, where the breakage of  $C_5-C_6$  bond produces an alkyl radical S7 ( $\Delta E_a = 5.9$   
437 kcal/mol.). The other is cyclization reaction, where the attack of oxygen atom of  
438 O-centered site on the C4-site of the  $C_3=C_4$  double bond generates the ring-retaining  
439 alkyl radical S15 ( $E_a = 8.0$  kcal/mol). The branching ratios for the formation of S7 and  
440 S15 are predicted to be 74.7% and 25.3%, respectively.

441 As shown in Figure 3, S7 decomposes through the barrierless rupture of -O-O-  
442 bridge bond to form alkoxy radical S8-x, which includes five possible conformers as  
443 presented in Figure S8. The Boltzmann populations of different conformers are listed  
444 in Table S4. S8-x can undergo various intramolecular H-shifts, in which a hydrogen  
445 atom is transferred from different carbon atoms to O-centered site, forming the alkyl  
446 radicals. Among the competing H-shift reactions, 1,5 H-shift occurring at the -  
447  $C_5(O)H$  group exhibits the smallest barrier ( $\Delta E_a = 0.6$  kcal/mol), and  $k_{MC-TST}$  is  
448 calculated to be  $8.2 \times 10^9$  s<sup>-1</sup> at ambient temperature (Table S5). The formed S8-c-P  
449 can readily isomerize to S9 due to its resonance stabilized structure. The unimolecular  
450 decomposition of S9 can proceed through the C1-C2 bond scission to produce a  
451 ketene-enol S10 and an alkyl radical S10-1 ( $\Delta E_a = 16.1$  kcal/mol), followed by  
452 reaction with  $O_2$  leading to a  $HO_2$  radical and a 1,2-dicarbonyl compound S10-2 ( $\Delta E_a$   
453 = 14.0 kcal/mol). Alternatively, S9 may undergo via the elimination of CO to generate  
454 an alkyl radicals S11 ( $\Delta E_a = 29.4$  kcal/mol). The aforementioned results show that the  
455 formation of S10 and S10-1 is energetically favorable, with the rate coefficient  $k_{S10}$  of  
456 26.1 s<sup>-1</sup>.

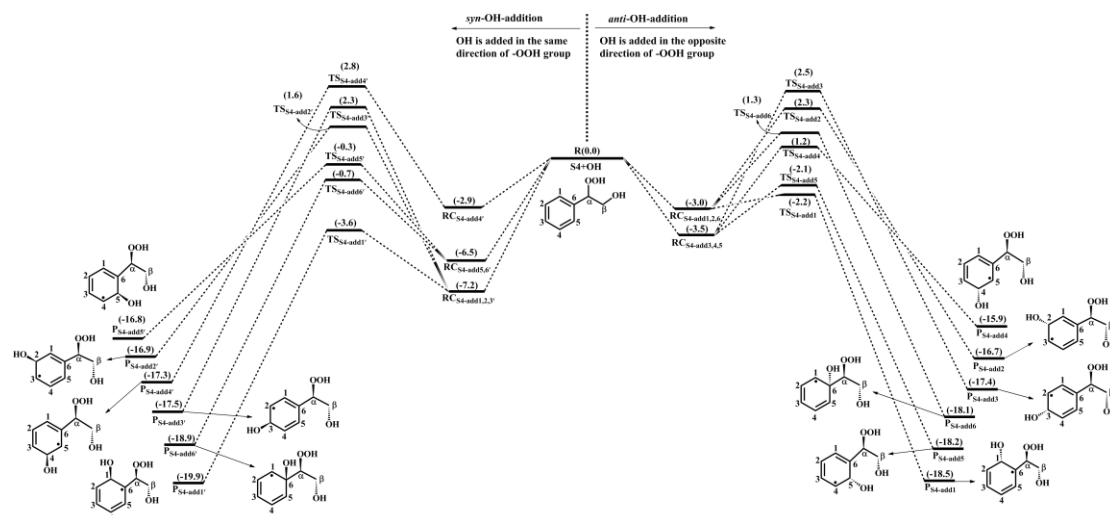
457 In the presence of  $O_2$ , the attack of an  $O_2$  molecule on the C-centered sites of S9

458 leads to the fourth generation peroxy radical S12-x ( $\Delta E_r > -20.5$  kcal/mol). Adopting  
459 the rate coefficient  $k_{R+O_2}$  of  $6.0 \times 10^{-12}$  cm<sup>3</sup> molecule<sup>-1</sup> s<sup>-1</sup> for the reactions of alkyl  
460 radicals with O<sub>2</sub>, and the atmospheric O<sub>2</sub> concentration of  $5 \times 10^{18}$  molecule cm<sup>-3</sup> (Ma  
461 et al., 2021), the pseudo-first-order rate constant  $k'_{R+O_2} = k_{R+O_2} [O_2]$  is  $3.0 \times 10^7$  s<sup>-1</sup>.  
462 The unimolecular decomposition of alkyl radicals is competitive only when their  
463 decay rate exceeds  $3.0 \times 10^7$  s<sup>-1</sup>.  $k'_{R+O_2}$  is about six orders of magnitude greater than  
464  $k_{S10}$ , indicating that the unimolecular decomposition of S9 is less importance. As  
465 shown in Figure S9, S12-x can proceed various intramolecular H-shift reactions,  
466 where hydrogen atom migrates from the different carbon sites or hydroxyl groups to  
467 the terminal oxygen atom of the -OO group, resulting in the formation of QOOH  
468 radicals and alkoxy radicals. Among these competing H-shift reactions, the 1,7-H  
469 transfer at the C $\alpha$ -site leading to the formation of S12-d-P exhibits the smallest barrier  
470 ( $\Delta E_a = 17.4$  kcal/mol). Then, it decomposes to yield an OH radical and a closed-shell  
471 product S13 containing a hydroperoxide, three hydroxyl and three carbonyl groups  
472 ( $\Delta E_a = 1.1$  kcal/mol).

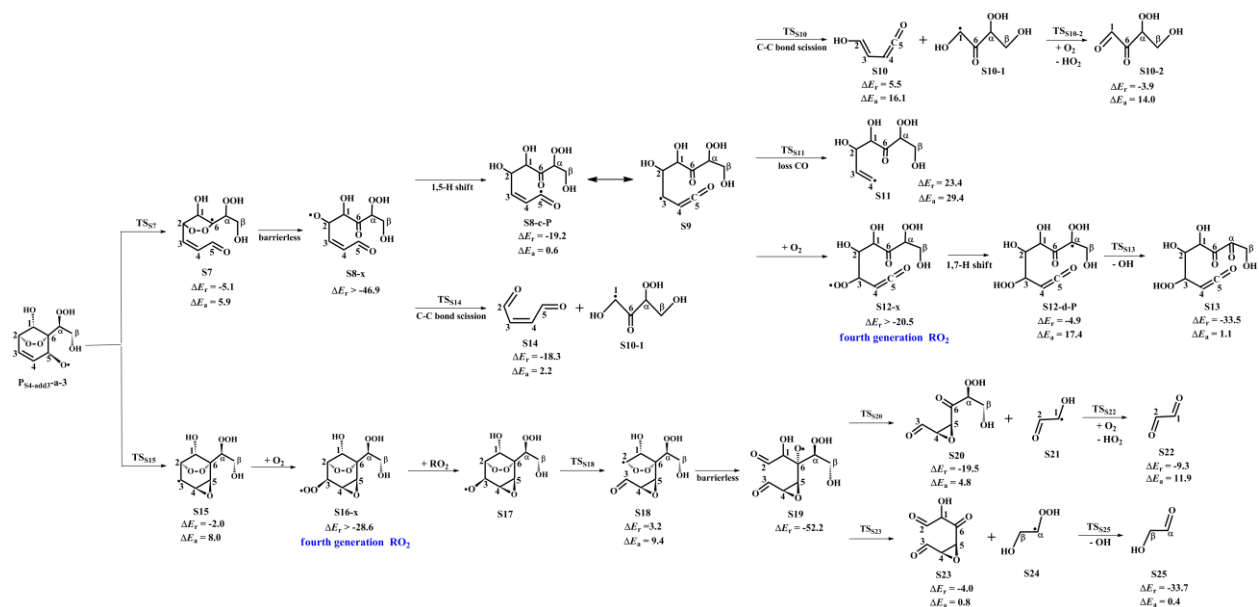
473 S8-x can proceed through the C<sub>1</sub>-C<sub>2</sub> bond scission to yield an unsaturated  
474 1,4-dicarbonyl species S14 and an alkyl radical S10-1 ( $\Delta E_a = 2.2$  kcal/mol), with the  
475 rate coefficient of  $2.1 \times 10^{10}$  s<sup>-1</sup>. Notably, both the 1,5 aldehyde H-shift and C<sub>1</sub>-C<sub>2</sub>  
476 bond scission reactions yield a closed-shell species S10-2 with up to five oxygen  
477 atoms, and the branching ratios are predicted to be 28.1% and 71.9%, respectively.  
478 The result is further supported by the previous study that the proportion of aldehyde  
479 H-shift products constitutes about one third of the total products in the reaction  
480 benzene + OH (Wang et al., 2020).

481 As shown in Figure 3, S15 can further react with O<sub>2</sub> leading to the fourth  
482 generation peroxy radical S16-x, which can proceed either intramolecular H-shifts  
483 forming QOOH radicals (Figure S10), or reactions with RO<sub>2</sub> radicals and NO forming  
484 alkoxy radical S17. Notably, the barriers of intramolecular H-shifts are extremely  
485 high ( $\Delta E_a > 34.6$  kcal/mol), making them less importance in the atmosphere. The  
486 transformation of S17 undergoes through the breakage of C<sub>2</sub>-C<sub>3</sub> bond to produce an  
487 alkyl radical S18 ( $\Delta E_a = 9.4$  kcal/mol), followed by fragmentation into an alkoxy

488 radical S19 via the barrierless rupture of the -O-O- bridge bond. Then, S19 dissociates  
 489 to an OH radical, a glycolaldehyde S25 and a C<sub>6</sub>-epoxide product S23 bearing a  
 490 hydroxy and three carbonyl groups, being the dominant pathway. The regeneration of  
 491 OH radicals drives the successive autoxidation of styrene, eventually leading to  
 492 the production of multifunctional products.



493  
 494 **Figure 2.** PES for the oxidation of 1<sup>st</sup>-ROOH(S4) initiated by OH radicals at the  
 495 M06-2X/6-311++G(3df,3pd)/M06-2X/6-31+g(d,p) level  
 496



497  
 498 **Figure 3.** PES for the unimolecular decomposition of P<sub>S4-add3-a-3</sub> and its subsequent reactions at  
 499 the M06-2X/6-311++G(3df,3pd)/M06-2X/6-31+g(d,p) level

500 **3.2.2 The oxidation mechanism of 1<sup>st</sup>-RONO<sub>2</sub> initiated by OH**  
 501 **radicals**

502 The OH-initiated oxidation of 1<sup>st</sup>-RONO<sub>2</sub> (S5) proceeds through the addition of  
503 OH radicals to different carbon sites in the benzene ring to form various alkyl radicals  
504 P<sub>S5-addx</sub>, as depicted in Figure 4. Among the competing OH-addition reactions, the  
505 OH-addition reaction at the C1-site, which proceeds on the opposite direction as the –  
506 ONO<sub>2</sub> group, has the smallest barrier (R<sub>S5-add1</sub>, ΔE<sub>a</sub> = 0.4 kcal/mol) due to the stability  
507 of the formed product P<sub>S5-add1</sub>. The result again shows that the *ortho*-addition reaction  
508 is energetically feasible. P<sub>S5-add1</sub> may isomerize to two other resonance structures,  
509 namely, P<sub>S5-add2</sub> and P<sub>S5-add3</sub>. For the reaction P<sub>S5-add1</sub> + O<sub>2</sub>, O<sub>2</sub> may add on either the  
510 opposite (*anti*-O<sub>2</sub>-addition) or the same direction (*syn*-O<sub>2</sub>-addition) relative to the –  
511 NO<sub>3</sub> group, leading to the second generation peroxy radicals P<sub>S5-add1-a</sub> and P<sub>S5-add1-s</sub>  
512 (Figure S11). The exoergicity of these two reactions are -6.7 and -4.4 kcal/mol,  
513 respectively, suggesting that the *anti*-O<sub>2</sub>-addition reaction is thermochemically  
514 favorable. Next, they can isomerize via a cyclization process to yield P<sub>S5-add1-a-1</sub> and  
515 P<sub>S5-add1-s-1</sub> with the ΔE<sub>a</sub> of 13.3 and 18.1 kcal/mol. This result shows that the  
516 cyclization reaction of *anti*-O<sub>2</sub>-addition product P<sub>S5-add1-a</sub> is kinetically feasible. A  
517 similar conclusion is also obtained from the reaction P<sub>S5-add3</sub> + O<sub>2</sub> that the formation of  
518 *anti*-O<sub>2</sub>-addition product P<sub>S5-add3-a-1</sub> is dominant. Due to the existence of the  
519 conjugate double bond, it facilitates the tautomerization between P<sub>S5-add1-a-1</sub> and  
520 P<sub>S5-add3-a-1</sub>. Therefore, we mainly focus on the subsequent chemistry of P<sub>S5-add3-a-1</sub> in  
521 the present study.

522 P<sub>S5-add3-a-1</sub> can further react with an O<sub>2</sub> molecule leading to the third generation  
523 peroxy radicals P<sub>S5-add3-a-2</sub>, which include multiple conformers. The lowest energy  
524 conformer resulting from conformer search is presented in Figure S12. In urban  
525 environments, the bimolecular reaction of P<sub>S5-add3-a-2</sub> with NO yields the second  
526 generation products, a bicyclic organic nitrate 2<sup>nd</sup>-RONO<sub>2</sub> (S26) and a BAR  
527 P<sub>S5-add3-a-3</sub>, as displayed in Figure S12. The detailed mechanism of OH-initiated  
528 oxidation of S26 is discussed in Section 3.3.2. As shown in Figure 5, P<sub>S5-add3-a-3</sub> can  
529 either proceed via a ring opening process to form an alkyl radical S27 (ΔE<sub>a</sub> = 7.3  
530 kcal/mol), or undergo through a cyclization process to generate an epoxide species  
531 S35 (ΔE<sub>a</sub> = 8.5 kcal/mol). The branching ratios of these two reactions are predicted to

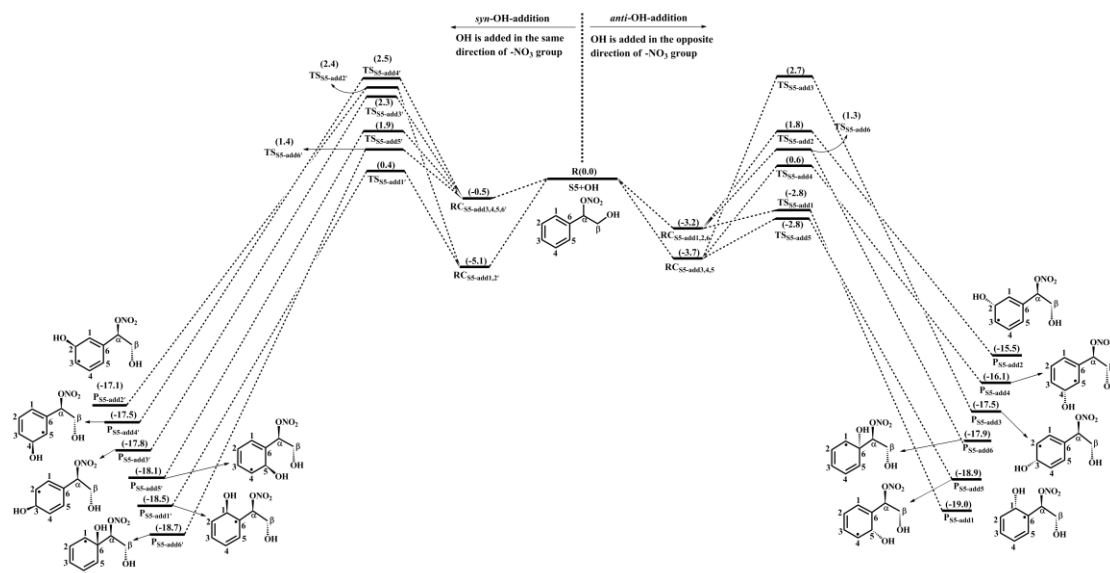
532 be 69.2% and 30.8%, respectively. Notably, the branching ratio of cyclization reaction  
533 of P<sub>S5-add3-a-3</sub> increases by 5.5% compared to that of cyclization reaction of  
534 P<sub>S4-add3-a-3</sub>, suggesting that the –ONO<sub>2</sub> substitution is beneficial to cyclization  
535 reaction.

536 The degradation of S27 proceeds through the barrierless scission of -O-O- bridge  
537 bond to form S28-x, and the Boltzmann populations of different conformers are listed  
538 in Table S6. S28-x can undergo via various intramolecular H-shifts to produce QOOH  
539 radicals, in which hydrogen atom transfer from the –C(O)H group to the terminal  
540 oxygen atom of the –OO group forming S28-e-P has the smallest barrier ( $\Delta E_a = 2.0$   
541 kcal/mol) (Figure S13). S28-e-P can readily isomerize to S29, which includes two  
542 distinct decomposition pathways. One is the C1-C2 bond cleavage, yielding a  
543 ketene-enol S30 and an alkyl radical S30-1 ( $\Delta E_a = 17.8$  kcal/mol), followed by  
544 reaction with O<sub>2</sub> to form a HO<sub>2</sub> radical and a 1,2-dicarbonyl species S30-2 ( $\Delta E_a =$   
545 11.7 kcal/mol). The other is the elimination of CO to generate an alkyl radical S31  
546 ( $\Delta E_a = 24.8$  kcal/mol), but the barrier is considerably high, making this pathway less  
547 competitive. The rate coefficient for the formation of S30 and S30-1 is calculated to  
548 be 14.4 s<sup>-1</sup>, which is about six orders of magnitude lower than the pseudo-first-order  
549 rate constant  $k'_{R+O_2}$ , indicating that the unimolecular decomposition of S29 is  
550 insignificant.

551 In the presence of O<sub>2</sub>, the bimolecular reaction of S29 with O<sub>2</sub> produces the  
552 fourth generation peroxy radicals S32-x, comprising five energetically similar  
553 conformers as shown in Figure S14. For the 1,7-H transfer reaction, hydrogen atom at  
554 the C $\alpha$ -site can be transferred through an eight-membered ring transition state to  
555 generate an alkyl radical S32-d-P ( $\Delta E_a = 23.3$  kcal/mol), followed by the elimination  
556 of NO<sub>2</sub> forming a closed product S33 ( $\Delta E_a = 1.0$  kcal/mol). S33 and S13 are isomeric  
557 species, with the former exhibiting more stability than the latter. S28-x can proceed  
558 through the cleavage of C<sub>1</sub>-C<sub>2</sub> bond to generate an unsaturated 1,4-dicarbonyl  
559 compound S34 and an alkyl radical S30-1. The rare coefficients of the 1,5 aldehyde  
560 H-shift and C1-C2 bond scission reactions are predicted to be  $1.7 \times 10^9$  and  $5.8 \times 10^9$   
561 s<sup>-1</sup> (Table S7), respectively, with the branching ratios of 23% and 77%. S30-1, formed

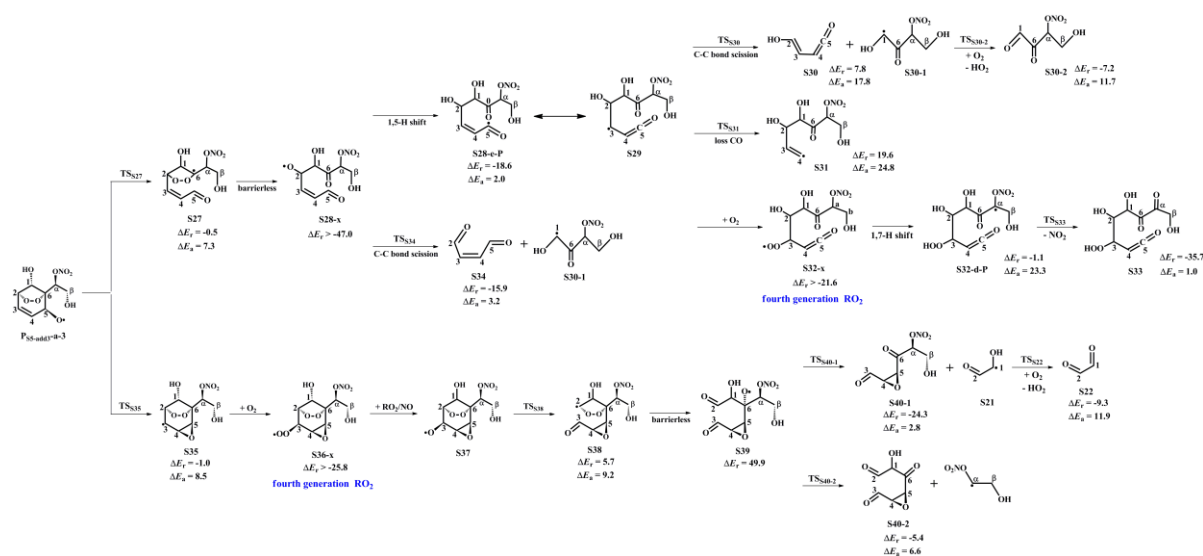
562 from the above mentioned two pathways, may undergo through H-abstraction by O<sub>2</sub>  
 563 to yield an organic nitrate S30-2 bearing a hydroxyl and two carbonyl groups ( $\Delta E_a =$   
 564 11.7 kcal/mol).

565 S35 can combine with an O<sub>2</sub> molecule forming the fourth generation peroxy  
 566 radicals S36-x, which have five possible conformers as shown in Figure S15. S36-x  
 567 can proceed either intramolecular H-shifts forming QOOH radicals, or reaction with  
 568 RO<sub>2</sub> radicals and NO generating alkoxy radical S37. However, the barriers of  
 569 intramolecular H-shifts are extremely high ( $\Delta E_a > 31.3$  kcal/mol), making them less  
 570 importance in the atmosphere. The degradation of S37 initially proceeds via the  
 571 breakage of C<sub>2</sub>-C<sub>3</sub> bond to form S38 ( $\Delta E_a = 9.2$  kcal/mol), followed by decomposition  
 572 into an alkoxy radical S39 via the barrierless scission of -O-O- bridge bond. The  
 573 dominant pathway of the unimolecular decomposition of S39 is the formation of a  
 574 glyoxal and a C<sub>6</sub>-epoxide species S40-1 bearing a -NO<sub>3</sub>, a hydroxyl and two carbonyl  
 575 groups. This process differs from the unimolecular decay of S19, where the favorable  
 576 pathways is the formation of a tricarbonyl compound S23. The aforementioned results  
 577 reveal that the preferable pathway is strongly dependent on the breakage of C-C bond  
 578 associated with the property of substituents in the decomposition of alkoxy radicals.



579  
 580 **Figure 4.** PES for the oxidation of 1<sup>st</sup>-RONO<sub>2</sub>(S5) initiated by OH radicals at the  
 581 M06-2X/6-311++G(3df,3pd)//M06-2X/6-31+g(d,p) level

582



583

584 **Figure 5.** PES for the unimolecular decomposition of P<sub>55</sub>-add<sub>3</sub>-a-3 and its subsequent reactions at  
 585 the M06-2X/6-311++G(3df,3pd)//M06-2X/6-31+g(d,p) level

586 **3.3 Third generation OH oxidation mechanisms of 2<sup>nd</sup>-ROOH**  
 587 **and 2<sup>nd</sup>-RONO<sub>2</sub>**

588 The second generation products, bicyclic hydroperoxide 2<sup>nd</sup>-ROOH and bicyclic  
 589 organic nitrate 2<sup>nd</sup>-RONO<sub>2</sub>, have multiple possible conformers. The global minimum  
 590 structures of 2<sup>nd</sup>-ROOH (S6) and 2<sup>nd</sup>-RONO<sub>2</sub> (S26) resulting from the conformer  
 591 search are presented in Figures S7 and S12, respectively.

592 **3.3.1 The oxidation mechanism of 2<sup>nd</sup>-ROOH initiated by OH**  
 593 **radicals**

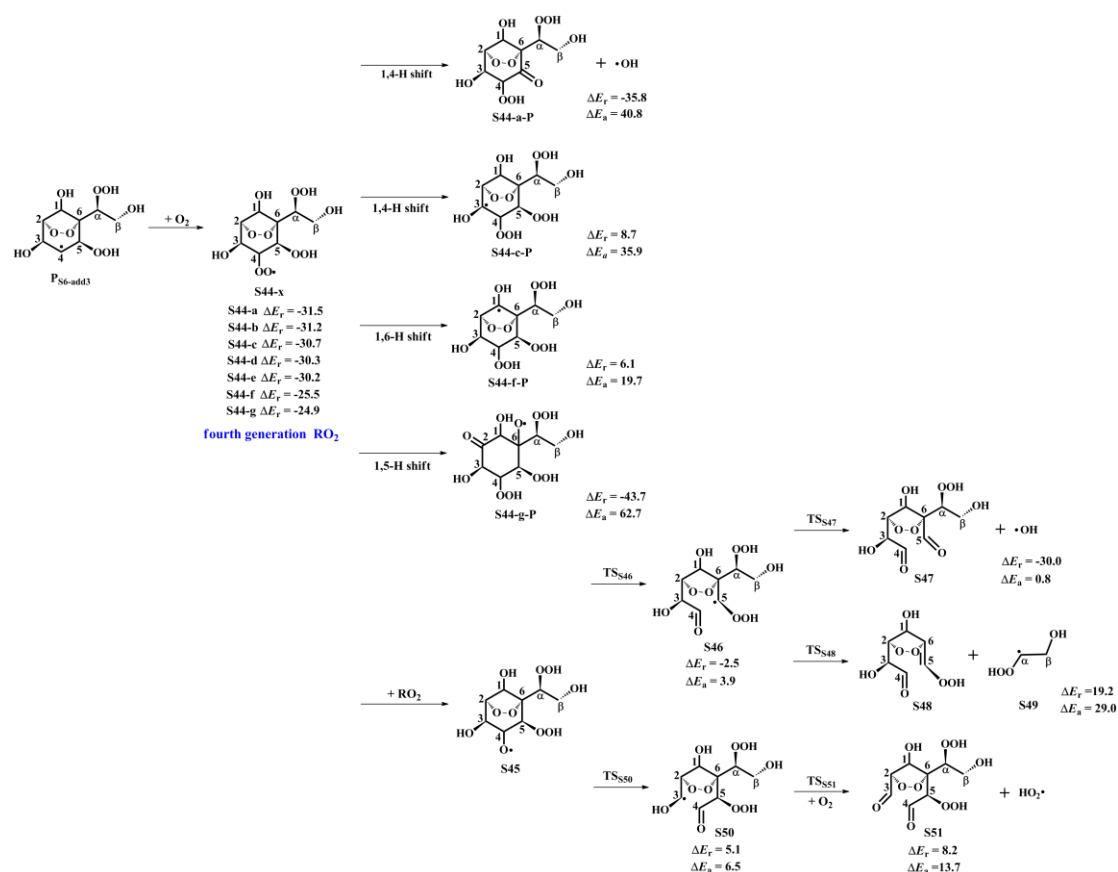
594 OH-initiated oxidation of 2<sup>nd</sup>-ROOH (S6) can either undergo through the  
 595 addition of OH radicals to either side of the C<sub>3</sub>=C<sub>4</sub> double bond to generate the alkyl  
 596 radicals, or proceed via H-abstraction from the different carbon sites to produce the  
 597 alkyl radicals and alkoxy radicals, as shown in Figures S16 and S17. For the  
 598 OH-addition reactions, *syn*-OH-addition is defined as the addition of OH radicals on  
 599 the same side as the -OOH group, while *anti*-OH-addition is referred to the addition  
 600 of OH radicals on the opposite side as the -OOH group. The addition of OH radicals  
 601 to the C3-site of the C<sub>3</sub>=C<sub>4</sub> double bond forming the product P<sub>S6-abs3</sub> has the smallest  
 602 barrier (ΔE<sub>a</sub> = 2.4 kcal/mol) and the exoergicity of -33.5 kcal/mol. For the  
 603 H-abstraction reactions, the abstraction of hydrogen atom at the C5-site is the most

604 favorable pathway ( $\Delta E_a = 3.6$  kcal/mol) and the exoergicity of  $-20.2$  kcal/mol. It is  
605 mainly because that the presence of an allyl group enhances the stability of the  
606 resulting product  $P_{S6-abs5}$ . Notably, the abstraction of hydrogen atom at the C2-site  
607 proceeds through a concerted process of C<sub>2</sub>-H bond and -O-O- bridge bond rupture,  
608 leading to the formation of an alkoxy radical  $P_{S6-abs2}$  ( $\Delta E_a = 7.2$  kcal/mol). This  
609 reaction is expected to be less importance due to its higher energy barrier. The rate  
610 coefficient of the favorable OH-addition reaction is calculated to be  $6.4 \times 10^{-11}$  cm<sup>3</sup>  
611 molecule<sup>-1</sup> s<sup>-1</sup>, which is about one order of magnitude greater than that of the  
612 preferable H-abstraction reaction ( $4.1 \times 10^{-12}$  cm<sup>3</sup> molecule<sup>-1</sup> s<sup>-1</sup>). Based on the above  
613 discussion, it can be concluded that OH-addition reaction is favorable on both  
614 thermochemically and kinetically. This conclusion is further supported by the OH +  
615 alkene reaction systems that OH-addition pathways are predominant (Chen et al.,  
616 2021; Yang et al., 2017; Arathala and Musah, 2024).

617 As depicted in Figure S18, the unimolecular decay of the product  $P_{S6-add3}$   
618 resulting from the favorable OH-addition reaction proceeds through a cyclization  
619 process to yield an epoxide compound S41 and an OH radical byproduct with the  $\Delta E_a$   
620 of  $15.3$  kcal/mol and the rate coefficient  $k_{R41}$  of  $1.8 \times 10^2$  s<sup>-1</sup>, or undergoes via  
621 intramolecular 1,4 H-shift to form a peroxy radical S42 with the  $\Delta E_a$  of  $21.8$  kcal/mol  
622 and the rate coefficient  $k_{R43}$  of  $1.9$  s<sup>-1</sup>, or proceeds via the elimination of hydrogen  
623 atom to produce an alkene S43 with the  $\Delta E_a$  of  $37.9$  kcal/mol. Based on the values of  
624  $\Delta E_a$  and the corresponding rate coefficients, the dominant pathway of the  
625 unimolecular decomposition of  $P_{S6-add3}$  is the formation of S41. In the presence of O<sub>2</sub>,  
626 the pseudo-first-order rate constant  $k'_{R+O_2}$  of the reactions of alkyl radicals with O<sub>2</sub> is  
627  $3.0 \times 10^7$  s<sup>-1</sup>, which is about five orders of magnitude greater than  $k_{R41}$ , suggesting  
628 that the unimolecular decomposition of  $P_{S6-add3}$  is insignificant.

629 As shown in Figure 6, the fourth generation peroxy radicals S44-x formed in the  
630 addition reaction  $P_{S6-add3} + O_2$  can either proceed via intramolecular H-shifts to form  
631 QOOH, or undergo through self- or cross-reactions to yield an alkoxy radical S45.  
632 Due to the considerably high barriers of intramolecular H-shifts, they are deemed to  
633 be negligible under atmospheric conditions. S45 can convert into an alkyl radical S46

634 through the cleavage of C<sub>4</sub>-C<sub>5</sub> bond, or dissociate to an alkyl radical S50 via the  
 635 rupture of C<sub>3</sub>-C<sub>4</sub> bond. The barrier of the former reaction is 3.9 kcal/mol, which is  
 636 lower than that of the latter pathway by 2.6 kcal/mol, indicating that the formation of  
 637 S46 is kinetically preferable. Then, S46 decomposes into an OH radical byproduct  
 638 and a C<sub>8</sub>-product S47 bearing a -OOH, a peroxide bridge, two carbonyls, and three  
 639 hydroxy groups, which is expected to be the dominant pathway owing to its lower  
 640 barrier. The rate coefficient  $k_{RS47}$  is estimated to be  $1.8 \times 10^9 \text{ s}^{-1}$ , which is about two  
 641 orders of magnitude greater than the pseudo-first-order rate constant  $k'_{R+O_2}$  ( $3.0 \times 10^7$   
 642  $\text{s}^{-1}$ ). The result reveals that the unimolecular decomposition of S46 is more  
 643 competitive than the bimolecular reaction with O<sub>2</sub>. The formed OH radicals can once  
 644 again participate in the oxidations of styrene and its multifunctional products,  
 645 continuing these processes until they are completely consumed.



646  
 647 **Figure 6.** PES for the subsequent reactions of P<sub>S6-add3</sub> in the presence of O<sub>2</sub> at the  
 648 M06-2X/6-311++G(3df,3pd)//M06-2X/6-31+g(d,p) level

649 **3.3.2 The oxidation mechanism of 2<sup>nd</sup>-RONO<sub>2</sub> initiated by OH**  
 650 **radicals**

651 OH-initiated oxidation of 2<sup>nd</sup>-RONO<sub>2</sub> (S26) includes four different OH-addition  
652 pathways and five different H-abstraction pathways, as displayed in Figures S19 and  
653 S20. For the OH-addition reactions, the attack of OH radicals on the C3-site of the  
654 C<sub>3</sub>=C<sub>4</sub> double bond forming the product P<sub>S26-add3</sub>, occurring on the same direction  
655 relative to the -ONO<sub>2</sub> group, is found to be the favorable pathway ( $\Delta E_a = 2.4$   
656 kcal/mol,  $\Delta E_r = -33.6$  kcal/mol). For the H-abstraction reactions, the abstraction of  
657 hydrogen atom at the C5-site is identified as the preferable pathway ( $\Delta E_a = 5.7$   
658 kcal/mol,  $\Delta E_r = -20.1$  kcal/mol) due to the enhanced stability of the resulting product  
659 P<sub>S26-add5</sub> by the presence of an allyl group. By comparing the values of  $\Delta E_a$  and  $\Delta E_r$  of  
660 the favorable OH-addition and H-abstraction pathways, it can be concluded that the  
661 former case is dominant on both thermochemically and kinetically. This conclusion is  
662 consistent with the result from the reaction 2<sup>nd</sup>-ROOH (S6) + OH that OH-addition is  
663 more competitive than H-abstraction.

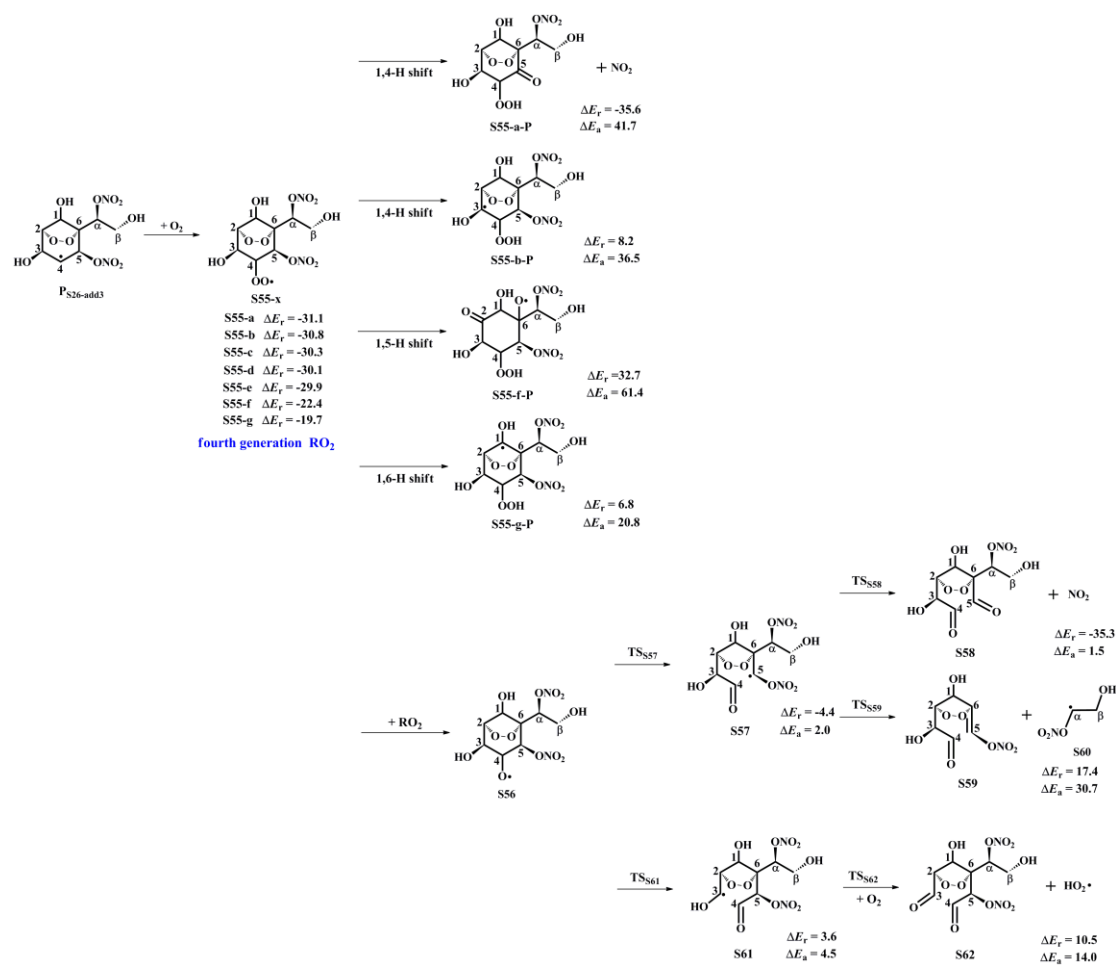
664 The product P<sub>S26-add3</sub> arising from the favorable OH-addition pathway has three  
665 potential unimolecular decay pathways, as depicted in Figure S21: (1) P<sub>S26-add3</sub>  
666 dissociates to an epoxide S52 and a NO<sub>2</sub> molecule through a cyclization process with  
667 the  $\Delta E_a$  of 18.5 kcal/mol and the rate coefficient  $k_{R52}$  of 0.4 s<sup>-1</sup>; (2) P<sub>S26-add3</sub> isomerizes  
668 to an alkyl radical S53 via the intramolecular 1,2 H-shift ( $\Delta E_a = 40.0$  kcal/mol); (3)  
669 P<sub>S26-add3</sub> converts into an alkene S54 via the elimination of hydrogen atom ( $\Delta E_a = 39.1$   
670 kcal/mol). Based on the value of  $\Delta E_a$  and the corresponding rate coefficient, the  
671 dominant pathway of the unimolecular decomposition of P<sub>S26-add3</sub> is the formation of  
672 S52.  $k_{R52}$  is about seven orders of magnitude lower than the pseudo-first-order rate  
673 constant  $k'_{R+O_2}$ , indicating that the unimolecular decomposition of P<sub>S26-add3</sub> is less  
674 importance.

675 In the presence of O<sub>2</sub>, P<sub>S26-add3</sub> can react with an O<sub>2</sub> molecule leading to the  
676 formation of the fourth generation peroxy radicals S55-x, comprising seven possible  
677 conformers as shown in Figure 7. For the intramolecular H-shifts of S55-x, not all of  
678 reactants (S55-c, S55-d and S55-e) have the suitable conformers that allow for the  
679 pathways across the reaction barriers. The barriers of intramolecular H-shifts are  
680 considerably high ( $\Delta E_a = 20.8$  kcal/mol), making them uncompetitive in the

681 atmosphere. Alternatively, S55-x can react with other RO<sub>2</sub> radicals forming an alkoxy  
682 radical S56, followed by decomposition into an alkyl radical S57 via the breakage of  
683 C<sub>4</sub>-C<sub>5</sub> bond ( $\Delta E_a = 2.0$  kcal/mol), or fragmentation into an alkyl radical S61 through  
684 the cleavage of C<sub>3</sub>-C<sub>4</sub> bond ( $\Delta E_a = 4.5$  kcal/mol). The aforementioned results reveal  
685 that the formation of S57 is energetically favorable, which is consistent with the  
686 conclusion derived from the unimolecular decomposition of S45 that the breakage of  
687 C<sub>4</sub>-C<sub>5</sub> bond is feasible. Next, S57 dissociates to a NO<sub>2</sub> coproduct and a C<sub>8</sub>-product  
688 S58 that possessed a -NO<sub>3</sub>, a peroxide bridge, two carbonyls, and three hydroxy  
689 groups. This pathway is expected to be the dominant one ( $\Delta E_a = 1.5$  kcal/mol), with  
690 the rate coefficient  $k_{RS58}$  of  $1.2 \times 10^9$  s<sup>-1</sup>. The resulting NO<sub>2</sub> can further participate in  
691 the cycling of NO<sub>x</sub>, ultimately generating tropospheric ozone and SOA.

692 The overall reaction mechanism and the fractional yields of the major products in  
693 the multi-generation OH oxidation of styrene under different NO<sub>x</sub> conditions are  
694 presented in Figures S22 and S23. In the low-NO<sub>x</sub> conditions, the fractional yield of  
695 the first generation closed-shell product 1<sup>st</sup>-ROOH (S4) formed from the reaction  
696 S2-1-x + HO<sub>2</sub> · is predicted to be 71.6%. For the second generation OH oxidation, the  
697 reaction of the peroxy radical P<sub>S4-add3-a-2</sub> with HO<sub>2</sub> radicals produces the second  
698 generation closed-shell product 2<sup>nd</sup>-ROOH (S6) and an alkoxy radical P<sub>S4-add3-a-3</sub>,  
699 with the fractional yields of 41.4% and 10.4%, respectively. The formed P<sub>S4-add3-a-2</sub>  
700 can either proceed through the C<sub>5</sub>-C<sub>6</sub> bond scission to produce an alkyl radical S7 with  
701 the fractional yield of 7.8%, or undergo via a cyclization process to generate an alkyl  
702 radical S15 with the fractional yield of 2.6%. S7 and S15 can be transformed via a  
703 series of reactions, ultimately leading to the formation of second generation  
704 closed-shell product S10-2, S13 and S23, with the fractional yields of 5.6%, 2.2% and  
705 1.3%, respectively. For the third generation OH oxidation, the degradation of  
706 2<sup>nd</sup>-ROOH (S6) ultimately yields the third generation closed-shell products S47 and  
707 S51, with the fractional yields of 26.3% and 0.3%, respectively. As a result, the major  
708 closed-shell products are 1<sup>st</sup>-ROOH (S4), 2<sup>nd</sup>-ROOH (S6), S10-2, S13 and S47 in the  
709 multi-generation OH oxidation of styrene in the low-NO<sub>x</sub> conditions.

710 In the high-NO<sub>x</sub> conditions, the fractional yield of the first generation  
711 closed-shell product 1<sup>st</sup>-RONO<sub>2</sub> (S5) formed from the reaction S2-1-x + NO is  
712 predicted to be 26.5%, as shown in Figure S23. As the OH oxidation reactions  
713 proceed, 1<sup>st</sup>-RONO<sub>2</sub> (S5) can be initially transformed into the peroxy radical  
714 P<sub>S5-add3-a-2</sub>, followed by reaction with NO to form the second generation closed-shell  
715 product 2<sup>nd</sup>-RONO<sub>2</sub> (S26) and an alkoxy radical P<sub>S5-add3-a-3</sub>, with the fractional  
716 yields of 4.8% and 11.2%, respectively. The decomposition of P<sub>S5-add3-a-3</sub> undergoes  
717 via two distinct pathways. One is the C<sub>5</sub>-C<sub>6</sub> bond cleavage, leading to an alkyl radical  
718 S27 with the fractional yield of 7.8%. The other is the cyclization, resulting in an  
719 alkyl radical S35 with the fractional yield of 3.4%. The resulting S27 and S35  
720 undergo multiple oxidation steps, finally leading to the formation of the second  
721 generation closed-shell products S30-2, S33 and S40-1, with the fractional yields of  
722 6.0%, 1.8%, and 1.7%, respectively. 2<sup>nd</sup>-RONO<sub>2</sub> (S26) can be further oxidized to  
723 yield the third generation closed-shell products S58 and S62, with the fractional yields  
724 of 2.6% and 0.03%, respectively. In summary, the major closed-shell products are  
725 1<sup>st</sup>-RONO<sub>2</sub> (S5), 2<sup>nd</sup>-RONO<sub>2</sub> (S26), S30-2 and S58 in the multi-generation OH  
726 oxidation of styrene in the high-NO<sub>x</sub> conditions.



727

728 **Figure 7.** PES for the subsequent reactions of  $\text{P}_{\text{S26-add3}}$  in the presence of  $\text{O}_2$  at the  
 729 M06-2X/6-311++G(3df,3pd)//M06-2X/6-31+g(d,p) level

### 730 3.4 Volatility classes

731 The volatility classes for various organic compounds are based on their  
 732 saturation concentration, as proposed by Donahue et al. (2012). The saturated vapour  
 733 pressure ( $P^0$ ) and saturated concentration ( $c^0$ ) of styrene and its multi-generation OH  
 734 oxidation products are predicted by using the SIMPOL.1 method (Pankow et al.,  
 735 2008). As show in Table S8, the  $P^0$  and  $c^0$  of the first generation closed-shell product  
 736 benzaldehyde ( $\text{C}_7\text{H}_6\text{O}$ ) are  $7.62 \times 10^{-4}$  atm and  $2.89 \times 10^6$  ug/m<sup>3</sup>, respectively, which  
 737 are 3-4 orders of magnitude greater than those of S4 ( $\text{C}_8\text{H}_{10}\text{O}_3$ ,  $P^0 = 1.43 \times 10^{-7}$  atm  
 738 and  $c^0 = 8.89 \times 10^2$  ug/m<sup>3</sup>) and S5 ( $\text{C}_8\text{H}_9\text{NO}_3$ ,  $P^0 = 2.54 \times 10^{-7}$  atm and  $c^0 = 1.87 \times$   
 739  $10^3$  ug/m<sup>3</sup>). Based on the values of  $c^0$ , benzaldehyde is classified as the volatile  
 740 organic compounds (VOCs), whereas S4 and S5 are classified as the intermediate  
 741 volatility organic compounds (IVOCs). These first generation closed-shell products  
 742 exist exclusively in the gas phase under atmospheric conditions (Bianchi et al., 2019).

743 For the second generation closed-shell products, S6 ( $C_8H_{12}O_8$ ,  $c^0 = 4.50 \times 10^{-2}$   
744  $ug/m^3$ ) and S26 ( $C_8H_{10}N_2O_{10}$ ,  $c^0 = 0.18 ug/m^3$ ) formed from the bimolecular reactions  
745 with  $HO_2$  radicals and NO are classified as the low volatility organic compounds  
746 (LVOCs). Similarly, S13 ( $C_8H_{10}O_8$ ,  $c^0 = 2.97 \times 10^{-2} ug/m^3$ ) and S33 ( $C_8H_{10}O_8$ ,  $c^0 =$   
747  $2.97 \times 10^{-2} ug/m^3$ ), formed through the ring-opening and subsequent intramolecular  
748 H-shift reactions of  $P_{S4-add3-a-3}$  and  $P_{S5-add3-a-3}$ , respectively, are also classified as  
749 LVOCs, which can condense onto the existing large particles (Bianchi et al., 2019).  
750 The  $c^0$  values of the remaining closed-shell products are significantly greater than  
751 those of the aforementioned four products, for example, the  $c^0$  values of S20 ( $C_6H_8O_6$ )  
752 and S40-1 ( $C_6H_7NO_7$ ), formed by the cyclization and decomposition reactions of  
753  $P_{S4-add3-a-3}$  and  $P_{S5-add3-a-3}$ , are 42.21 and 75.86  $ug/m^3$ , respectively, classifying them  
754 as the semivolatile organic compounds (SVOC).

755 For the third generation closed-shell products, the  $c^0$  values of S47 ( $C_8H_{12}O_9$ ,  $c^0$   
756  $= 2.68 \times 10^{-4} ug/m^3$ ) and S51 ( $C_8H_{10}O_{10}$ ,  $c^0 = 1.58 \times 10^{-4} ug/m^3$ ), formed through the  
757  $O_2$ -addition and subsequent decomposition reactions of  $P_{S6-add3}$ , are about two orders  
758 of magnitude lower than those of the second generation closed-shell products S6 and  
759 S13, despite being classified as LVOCs. Similarly, S58 ( $C_8H_{11}NO_{10}$ ,  $c^0 = 5.37 \times 10^{-4}$   
760  $ug/m^3$ ) and S62 ( $C_8H_{10}N_2O_{12}$ ,  $c^0 = 6.18 \times 10^{-4} ug/m^3$ ), formed via the  $O_2$ -addition and  
761 subsequent decomposition reactions of  $P_{S26-add3}$ , exhibit lower  $c^0$  values compared to  
762 the second generation closed-shell products S26 and S33. The aforementioned results  
763 reveal that the volatility of the multi-generation OH oxidation products significantly  
764 decreases with increasing the number of OH oxidation steps. As the oxidation  
765 reactions of the third generation closed-shell products proceed further, the formed  
766 products may possess sufficiently low volatility to participate in the formation and  
767 growth of new aerosol particle.

## 768 **4 Conclusions and atmospheric implications**

769 The results reveal that the first generation  $RO_2$  radicals, formed from the  
770 addition of OH radicals to the  $C_\beta$ -site of a vinyl group in styrene followed by  
771  $O_2$ -addition, can proceed intramolecular H-shifts to generate various alkyl and alkoxy

772 radicals. The rate coefficient  $k_{\text{MC-TST}}$  is calculated to be  $1.6 \times 10^{-4} \text{ s}^{-1}$ . Among the  
773 competing H-shift pathways, the hydrogen atom transfer from the  $-\text{OH}$  group to the  
774 terminal oxygen atom of the  $-\text{OO}$  group has the lowest barrier. The resulting alkoxy  
775 radical can further decompose into benzaldehyde through the successive elimination  
776 of HCHO and an OH radical. The 1,5-H shift reaction occurring at the  $-\text{OH}$  group is  
777 the rate-determining step in the formation of benzaldehyde. Alternatively, the first  
778 generation  $\text{RO}_2$  radicals can proceed bimolecular reactions with  $\text{HO}_2$  radicals and NO,  
779 leading to the formation of the first generation closed-shell C7- and C8-products  
780  $1^{\text{st}}\text{-ROOH}$  ( $\text{C}_8\text{H}_{10}\text{O}_3$ ), benzaldehyde ( $\text{C}_7\text{H}_6\text{O}$ ), and  $1^{\text{st}}\text{-RONO}_2$  ( $\text{C}_8\text{H}_9\text{NO}_3$ ).

781 For the second generation OH oxidation, OH-addition reaction occurring at the  
782 *ortho*-site of  $1^{\text{st}}\text{-ROOH}$  and  $1^{\text{st}}\text{-RONO}_2$  has a significant dominance. This is consistent  
783 with the analogous reaction systems, toluene + OH and phenol + OH, in which  
784 *ortho*-OH-addition reaction is energetically favorable (Wu et al., 2020; Xu and Wang,  
785 2013). The resulting alkyl radicals may undergo two  $\text{O}_2$ -addition steps and a  
786 cyclization process to form BPR, which can react with  $\text{HO}_2$  radicals and NO to yield  
787 the corresponding BAR, and the second generation closed-shell C8-product  
788  $2^{\text{nd}}\text{-ROOH}$  ( $\text{C}_8\text{H}_{12}\text{O}_8$ ) and  $2^{\text{nd}}\text{-RONO}_2$  ( $\text{C}_8\text{H}_{10}\text{N}_2\text{O}_{10}$ ), with the fractional yields of 41.4%  
789 and 4.8%. The unimolecular decomposition of BAR formed in the reaction  $1^{\text{st}}\text{-ROOH}$   
790 + OH includes two distinct pathways: (1) ring-opening and followed by  
791 decomposition, yielding the multifunctional products S10-2 ( $\text{C}_4\text{H}_6\text{O}_5$ ) and S13  
792 ( $\text{C}_8\text{H}_{10}\text{O}_8$ ) with the fractional yields of 5.6% and 2.2%, respectively; or (2) cyclization  
793 and followed by dissociation, generating the closed-shell C6-product S23 ( $\text{C}_6\text{H}_6\text{O}_5$ )  
794 with the fractional yield of 1.3%. The major products formed from the unimolecular  
795 decomposition of BAR in the reaction  $1^{\text{st}}\text{-RONO}_2$  + OH are the multifunctional  
796 products S30-2 ( $\text{C}_4\text{H}_5\text{NO}_6$ ), S33 ( $\text{C}_8\text{H}_{10}\text{O}_8$ ) and S40-1 ( $\text{C}_6\text{H}_7\text{NO}_7$ ), with the fractional  
797 yields of 6.0%, 1.8% and 1.7%, respectively.

798 For the third generation OH oxidation, the addition of OH radicals to the C=C  
799 bond in  $2^{\text{nd}}\text{-ROOH}$  and  $2^{\text{nd}}\text{-RONO}_2$  is the dominant pathway. The resulting alkyl  
800 radicals can proceed a series of reactions to produce the alkoxy radicals, which  
801 subsequently decompose into an OH radical byproduct and a closed-shell C<sub>8</sub>-product

802 S47 ( $C_8H_{12}O_9$ ), identified as the favorable pathway in the reaction  $2^{nd}$ -ROOH + OH.  
803 S47 contains a –OOH, a peroxide bridge, two carbonyls, and three hydroxy groups.  
804 The major product formed in the reaction  $2^{nd}$ -RONO<sub>2</sub> + OH is a closed-shell  
805 C<sub>8</sub>-product S58 ( $C_8H_{11}NO_{10}$ ), which contain a –NO<sub>3</sub>, a peroxide bridge, two carbonyls,  
806 and three hydroxy groups. The fractional yields of S47 and S58 are 26.3% and 2.6%,  
807 respectively. The volatility of the oxidation products significantly decreases with  
808 increasing the number of OH oxidation steps in the multi-generation OH oxidation  
809 of styrene.

810 In the laboratory chamber experiments, the structures of some specific oxidation  
811 products remain uncharacterized but are merely inferred from the exact mass and  
812 fragmentation data. Using high-level quantum chemistry methods, we identify the  
813 molecular structures of multifunctional products and elucidate their formation  
814 pathways in the multi-generation OH oxidation of styrene. The mechanistic insights  
815 derived from this work are broadly applicable to the photooxidation of structurally  
816 analogous aromatics. Furthermore, we quantify the yields of multifunctional products  
817 and demonstrate that their volatility decreases significantly with increasing the  
818 number of OH oxidation steps. The resulting multifunctional products may undergo a  
819 series of oxidation reactions to form low volatility compounds, thereby contributing to  
820 the formation and growth of new aerosol particle. In the future, more detailed  
821 experimental and theoretical studies need to be conducted to identify the molecular  
822 structures and formation pathways of multifunctional products formed through the  
823 photooxidation of other aromatics under both low and high-NO<sub>x</sub> conditions. These  
824 studies will facilitate a more accurate characterization of the chemical composition  
825 and formation yields of aromatic SOA, and thereby help narrow the gap between the  
826 measured and modeled SOA concentrations in urban environments.

827

## 828 **Data availability**

829 The data are accessible by contacting the corresponding author  
830 (huangyu@ieecas.cn).

831

## 832 **Supplement**

833 Tables S1 and S3 list the energy barriers of all the elementary reactions involved  
834 in the addition of OH radicals to styrene and 1<sup>st</sup>-ROOH (S4) predicted at different  
835 levels. Tables S2, S4 and S6 list the relative electronic energy, free energy and  
836 Boltzmann population of different conformers involved in S2-1-x, S8-x and S28-x.  
837 Tables S5 and S7 list the MC-TST rate coefficients for the intramolecular H-shift  
838 reactions of S8-x and S28-x. Table S8 summaries the saturated vapour pressure and  
839 saturated concentrations of styrene and its multiple generation OH oxidation  
840 closed-shell products. Figures S1-S3 display the PESs for the unimolecular reactions  
841 of S2-2-x, S2-3-x and S2-4-x. Figure S4 shows the global minimum structures of  
842 1<sup>st</sup>-ROOH(S4) and 1<sup>st</sup>-RONO<sub>2</sub>(S5). Figure S5 depicts the geometric parameters of  
843 toluene and 1<sup>st</sup>-ROOH (S4) and the NPA atomic charges of all the carbon atoms.  
844 Figures S6 and S11 show the PESs for the addition reactions P<sub>S4-add1</sub> + O<sub>2</sub> and P<sub>S5-add1</sub>  
845 + O<sub>2</sub>. Figures S7 and S12 present the lowest energy conformers of third generation  
846 peroxy radicals P<sub>S4-add3-a-2</sub> and P<sub>S5-add3-a-2</sub>. Figures S8-S10 depict the PESs for the  
847 intramolecular hydrogen transfer reactions of S8-x, S12-x and S16-x. Figures  
848 S13-S15 depict the PESs for the intramolecular hydrogen transfer reactions of S28-x,  
849 S32-x and S36-x. Figures S16-18 show the PESs for the OH-initiated oxidation of  
850 2<sup>nd</sup>-ROOH (S6) and unimolecular decomposition of P<sub>S6-add3</sub>. Figures S19-S21 show  
851 the PESs for the OH-initiated oxidation of 2<sup>nd</sup>-RONO<sub>2</sub> (S26) and unimolecular  
852 decomposition of P<sub>S26-add3</sub>. Figures S22 and S23 show the overall reaction mechanism  
853 of the multi-generation OH oxidation of styrene in the low- and high-NO<sub>x</sub> conditions.

854

## 855 **Author contribution**

856 LC and YH conceptualized the study. LC conducted quantum chemical  
857 calculation. YX and ZJ analyzed the data. LC conducted the volatility estimation. All  
858 authors discussed the results and commented on the manuscript.

859

## 860 **Competing interests**

861 The contact author has declared that none of the authors has any competing interests.

862

## 863 **Financial support**

864 This study was supported by the National Natural Science Foundation of China (grant  
865 nos. 42175134) and the Youth Innovation Promotion Association of the Chinese  
866 Academy of Sciences (grant number 2022415).

867

## 868 **Reference**

- 869 Alecu, I. M., Zheng, J., Zhao, Y., and Truhlar, D. G.: Computational thermochemistry: scale factor  
870 databases and scale factors for vibrational frequencies obtained from electronic model  
871 chemistries, *J. Chem. Theory Comput.*, 6, 2872-2887, <https://doi.org/10.1021/ct100326h>,  
872 2010.
- 873 Arathala, P., and Musah, R. A.: Atmospheric chemistry of chloroprene initiated by OH radicals:  
874 combined Ab initio/DFT calculations and kinetics analysis, *J. Phys. Chem. A*, 128,  
875 8983-8995, <https://doi.org/10.1021/acs.jpca.4c05428>, 2024.
- 876 Atkinson, R., and Arey, J.: Atmospheric degradation of volatile organic compounds, *Chem. Rev.*,  
877 103, 4605-4638, <https://doi.org/10.1021/cr0206420>, 2003.
- 878 Bianchi, F., Kurt n, T., Riva, M., Mohr, C., Rissanen, M. P., Roldin, P., Berndt, T., Crouse, J. D.,  
879 Wennberg, P. O., Mentel, T. F., Wildt, J., Junninen, H., Jokinen, T., Kulmala, M., Worsnop, D.  
880 R., Thornton, J. A., Donahue, N., Kjaergaard, H. G., and Ehn, M.: Highly oxygenated organic  
881 molecules (HOM) from gas-phase autoxidation involving peroxy radicals: a key contributor  
882 to atmospheric aerosol, *Chem. Rev.*, 119, 3472-3509,  
883 <https://doi.org/10.1021/acs.chemrev.8b00395>, 2019.
- 884 Bloss, C., Wagner, V., Jenkin, M. E., Volkamer, R., Bloss, W. J., Lee, J. D., Heard, D. E., Wirtz, K.,  
885 Martin-Reviejo, M., Rea, G., Wenger, J. C., and Pilling, M. J.: Development of a detailed  
886 chemical mechanism (MCMv3.1) for the atmospheric oxidation of aromatic hydrocarbons,  
887 *Atmos. Chem. Phys.*, 5, 641-664, <https://doi.org/10.5194/acp-5-641-2005>, 2005.
- 888 Boyd, A. A., Flaud, P. M., Daugey, N., and Lesclaux, R.: Rate constants for RO<sub>2</sub> + HO<sub>2</sub> reactions  
889 measured under a large excess of HO<sub>2</sub>, *J. Phys. Chem. A*, 107, 818-821,  
890 <https://doi.org/10.1021/jp026581r>, 2003.
- 891 Cabrera-Perez, D., Taraborrelli, D., Sander, R., and Pozzer, A.: Global atmospheric budget of  
892 simple monocyclic aromatic compounds, *Atmos. Chem. Phys.*, 16, 6931-6947,  
893 <https://doi.org/10.5194/acp-16-6931-2016>, 2016.
- 894 Canneaux, S., Bohr, F., and Henon, E.: KiSTheIP: a program to predict thermodynamic properties  
895 and rate constants from quantum chemistry results, *J. Comput. Chem.*, 35, 82-93,  
896 <https://doi.org/10.1002/jcc.23470>, 2013.
- 897 Chen, L., Huang, Y., Xue, Y., Jia, Z., and Wang, W.: Atmospheric oxidation of 1-butene initiated  
898 by OH radical: Implications for ozone and nitrous acid formations, *Atmos. Environ.*, 244,

899 118010-118021, <https://doi.org/10.1016/j.atmosenv.2020.118010>, 2021.

900 Cho, J., Roueintan, M., and Li, Z.: Kinetic and dynamic investigations of OH reaction with  
901 styrene, *J. Phys. Chem. A*, 118, 9460-9470, <https://doi.org/10.1021/jp501380j>, 2014.

902 Donahue, N. M., Kroll, J. H., Pandis, S. N., and Robinson, A. L.: A two-dimensional volatility  
903 basis set – Part 2: Diagnostics of organic-aerosol evolution, *Atmos. Chem. Phys.*, 12,  
904 615-634, <https://doi.org/10.5194/acp-12-615-2012>, 2012.

905 Eckart, C.: The penetration of a potential barrier by electrons, *Phys. Rev.*, 35, 1303-1309,  
906 <https://doi.org/10.1103/PhysRev.35.1303>, 1930.

907 Environmental Protection Agency (EPA). Clean Air Act: Title I-Air Pollution Prevention and  
908 Control. U.S. 1990.

909 Fernández-Ramos, A., Ellingson, B. A., Meana-Pañeda, R., Marques, J. M. C., and Truhlar, D. G.:  
910 Symmetry numbers and chemical reaction rates, *Theor. Chem. Acc.*, 118, 813-826,  
911 <https://doi.org/10.1007/s00214-007-0328-0>, 2007.

912 Forstner, H. J. L., Flagan, R. C., and Seinfeld, J. H.: Secondary organic aerosol from the  
913 photooxidation of aromatic hydrocarbons: molecular composition, *Environ. Sci. Technol.*, 31,  
914 1345-1358, <https://doi.org/10.1021/es9605376>, 1997.

915 Frisch, M. J., Trucks, G. W., Schlegel, H. B., Scuseria, G. E., Robb, M. A., Cheeseman, J. R.,  
916 Scalmani, G., Barone, V., Petersson, G. A., Nakatsuji, H., Li, X., Caricato, M., Marenich, A.  
917 V., Bloino, J., Janesko, B. G., Gomperts, R., Mennucci, B., Hratchian, H. P., Ortiz, J. V.,  
918 Izmaylov, A. F., Sonnenberg, J. L., Williams-Young, D., Ding, F., Lipparini, F., Egidi, F.,  
919 Goings, J., Peng, B., Petrone, A., Henderson, T., Ranasinghe, D., Zakrzewski, V. G., Gao, J.,  
920 Rega, N., Zheng, G., Liang, W., Hada, M., Ehara, M., Toyota, K., Fukuda, R., Hasegawa, J.,  
921 Ishida, M., Nakajima, T., Honda, Y., Kitao, O., Nakai, H., Vreven, T., Throssell, K.,  
922 Montgomery, J. A., Peralta, J. J. E., Ogliaro, F., Bearpark, M. J., Heyd, J. J., Brothers, E. N.,  
923 Kudin, K. N., Staroverov, V. N., Keith, T. A., Kobayashi, R., Normand, J., Raghavachari, K.,  
924 Rendell, A. P., Burant, J. C., Iyengar, S. S., Tomasi, J., Cossi, M., Millam, J. M., Klene, M.,  
925 Adamo, C., Cammi, R., Ochterski, J. W., Martin, R. L., Morokuma, K., Farkas, O., Foresman,  
926 J. B., and Fox, D. J.: Gaussian 16, Revision B.01, Gaussian, Inc., Wallingford CT, 2016.

927 Fu, Z., Guo, S., Xie, H. B., Zhou, P., Boy, M., Yao, M., and Hu, M.: A near-explicit reaction  
928 mechanism of chlorine-initiated limonene: implications for health risks associated with the  
929 concurrent use of cleaning agents and disinfectants, *Environ. Sci. Technol.*, 58, 19762-19773,  
930 <https://doi.org/10.1021/acs.est.4c04388>, 2024.

931 Fu, Z., Ma, F., Liu, Y., Yan, C., Huang, D., Chen, J., Elm, J., Li, Y., Ding, A., Pichelstorfer, L., Xie,  
932 H. B., Nie, W., Francisco, J. S., and Zhou, P.: An overlooked oxidation mechanism of toluene:  
933 computational predictions and experimental validations, *Chem. Sci.*, 14, 13050-13059,  
934 <https://doi.org/10.1039/D3SC03638C>, 2023.

935 Fu, Z., Xie, H. B., Elm, J., Guo, X., Fu, Z., and Chen, J.: Formation of low-volatile products and  
936 unexpected high formaldehyde yield from the atmospheric oxidation of methylsiloxanes,  
937 *Environ. Sci. Technol.*, 54, 7136-7145, <https://doi.org/10.1021/acs.est.0c01090>, 2020.

938 Fukui, K.: The path of chemical reactions - the IRC approach, *Acc. Chem. Res.*, 14, 363-368,  
939 <https://doi.org/10.1021/ar00072a001>, 1981.

940 Garmash, O., Rissanen, M. P., Pullinen, I., Schmitt, S., Kausiala, O., Tillmann, R., Zhao, D.,  
941 Percival, C., Bannan, T. J., Priestley, M., Hallquist, Å M., Kleist, E., Kiendler-Scharr, A.,  
942 Hallquist, M., Berndt, T., McFiggans, G., Wildt, J., Mentel, T. F., and Ehn, M.:

943 Multi-generation OH oxidation as a source for highly oxygenated organic molecules from  
944 aromatics, *Atmos. Chem. Phys.*, 20, 515-537, <https://doi.org/10.5194/acp-20-515-2020>, 2020.

945 Gilbert, R. G., and Smith, S. C.: Theory of unimolecular and recombination reactions, Blackwell  
946 Scientific: Carlton, Australia, 1990.

947 Glowacki, D. R., Liang, C. H., Morley, C., Pilling, M. J., and Robertson, S. H.: MESMER: an  
948 open-source master equation solver for multi-energy well reactions, *J. Phys. Chem. A*, 116,  
949 9545-9560, <https://doi.org/10.1021/jp3051033>, 2012.

950 Holbrook, K. A., Pilling, M. J., Robertson, S. H., and Robinson, P. J.: Unimolecular reactions, 2nd  
951 ed.; Wiley: New York, 1996.

952 Huang, Y., Su, T., Wang, L., Wang, N., Xue, Y., Dai, W., Lee, S. C., Cao, J., and Ho, S. S. H.:  
953 Evaluation and characterization of volatile air toxics indoors in a heavy polluted city of  
954 northwestern China in wintertime, *Sci. Total Environ.*, 662, 470-480,  
955 <https://doi.org/10.1016/j.scitotenv.2019.01.250>, 2019.

956 Iuga, C., Galano, A., and Vivier-Bunge, A.: Theoretical investigation of the OH-initiated oxidation  
957 of benzaldehyde in the troposphere, *Chem. Phys. Chem.*, 9, 1453-1459,  
958 <https://doi.org/10.1002/cphc.200800144>, 2008.

959 Iyer, S., Kumar, A., Savolainen, A., Barua, S., Daub, C., Pichelstorfer, L., Roldin, P., Garmash, O.,  
960 Seal, P., Kurt n, T., and Rissanen, M.: Molecular rearrangement of bicyclic peroxy radicals is  
961 a key route to aerosol from aromatics, *Nat. Commun.*, 14, 4984-4991,  
962 <https://doi.org/10.1038/s41467-023-40675-2>, 2023.

963 Ji, Y., Zhao, J., Terazono, H., Misawa, K., Levitt, N. P., Li, Y., Lin, Y., Peng, J., Wang, Y., Duan, L.,  
964 Pan, B., Zhang, F., Feng, X., An, T., Marrero-Ortiz, W., Secret, J., Zhang, A. L., Shibuya, K.,  
965 Molina, M. J., and Zhang, R.: Reassessing the atmospheric oxidation mechanism of toluene,  
966 *Proc. Natl. Acad. Sci. U.S.A.*, 114, 8169-8174, <https://doi.org/10.1073/pnas.1705463114>,  
967 2017.

968 Koppmann, R.: Volatile organic compounds in the atmosphere, John Wiley & Sons, 2008.

969 Li, M., Zhang, Q., Zheng, B., Tong, D., Lei, Y., Liu, F., Hong, C., Kang, S., Yan, L., Zhang, Y., Bo,  
970 Y., Su, H., Cheng, Y., and He, K.: Persistent growth of anthropogenic non-methane volatile  
971 organic compound (NMVOC) emissions in China during 1990-2017: drivers, speciation and  
972 ozone formation potential, *Atmos. Chem. Phys.*, 19, 8897-8913,  
973 <https://doi.org/10.5194/acp-19-8897-2019>, 2019.

974 Lu, T.: Molclus program, Version 1.9.3. <http://www.keinsci.com/research/molclus.html> (accessed  
975 May 21, 2024).

976 Ma, F., Guo, X., Xia, D., Xie, H. B., Wang, Y., Elm, J., Chen, J., and Niu, J.: Atmospheric  
977 chemistry of allylic radicals from isoprene: a successive cyclization-driven autoxidation  
978 mechanism, *Environ. Sci. Technol.*, 55, 4399-4409, <https://doi.org/10.1021/acs.est.0c07925>,  
979 2021.

980 M ller, K. H., Berndt, T., and Kjaergaard, H. G.: Atmospheric autoxidation of amines, *Environ.*  
981 *Sci. Technol.*, 54, 11087-11099, <https://doi.org/10.1021/acs.est.0c03937>, 2020.

982 M ller, K. H., Otkj r, R. V., Hyttinen, N., Kurt n, T., and Kjaergaard, H. G.: Cost-effective  
983 implementation of multiconformer transition state theory for peroxy radical hydrogen shift  
984 reactions, *J. Phys. Chem. A*, 120, 10072-10087, <https://doi.org/10.1021/acs.jpca.6b09370>,  
985 2016.

986 Molteni, U., Bianchi, F., Klein, F., Haddad, I. E., Frege, C., Rossi, M. J., Dommen, J., and

987 Baltensperger, U.: Formation of highly oxygenated organic molecules from aromatic  
988 compounds, *Atmos. Chem. Phys.*, 18, 1909-1921, <https://doi.org/10.5194/acp-18-1909-2018>,  
989 2018.

990 Neese, F.: Software update: the ORCA program system—version 6.0, *Wires Comput. Mol. Sci.*, 15,  
991 e70019, <https://doi.org/10.1002/wcms.70019>, 2025.

992 Nie, W., Yan, C., Huang, D. D., Wang, Z., Liu, Y., Qiao, X., Guo, Y., Tian, L., Zheng, P., Xu, Z., Li,  
993 Y., Xu, Z., Qi, X., Sun, P., Wang, J., Zheng, F., Li, X., Yin, R., Dallenbach, K. R., Bianchi, F.,  
994 Petř T., Zhang, Y., Wang, M., Schervish, M., Wang, S., Qiao, L., Wang, Q., Zhou, M.,  
995 Wang, H., Yu, C., Yao, D., Guo, H., Ye, P., Lee, S., Li, Y. J., Liu, Y., Chi, X., Kerminen, V. M.,  
996 Ehn, M., Donahue, N. M., Wang, T., Huang, C., Kulmala, M., Worsnop, D., Jiang, J., and  
997 Ding, A.: Secondary organic aerosol formed by condensing anthropogenic vapours over  
998 China's megacities, *Nat. Geosci.*, 15, 255-261, <https://doi.org/10.1038/s41561-022-00922-5>,  
999 2022.

1000 Orlando, J. J., and Tyndall, G. S.: Laboratory studies of organic peroxy radical chemistry: an  
1001 overview with emphasis on recent issues of atmospheric significance, *Chem. Soc. Rev.*, 41,  
1002 6294-6317, <https://doi.org/10.1039/C2CS35166H>, 2012.

1003 Pankow, J. F., and Asher, W. E.: SIMPOL.1: a simple group contribution method for predicting  
1004 vapor pressures and enthalpies of vaporization of multifunctional organic compounds, *Atmos.*  
1005 *Chem. Phys.*, 8, 2773-2796, <https://doi.org/10.5194/acp-8-2773-2008>, 2008.

1006 Pasik, D., Frandsen, B. N., Meder, M., Iyer, S., Kurtić, T., and Myllys, N.: Gas-phase oxidation of  
1007 atmospherically relevant unsaturated hydrocarbons by acyl peroxy radicals, *J. Am. Chem.*  
1008 *Soc.*, 146, 13427-13437, <https://doi.org/10.1021/jacs.4c02523>, 2024.

1009 Sebbar, N., Bozzelli, J. W., and Bockhorn, H.: Thermochemistry and reaction paths in the  
1010 oxidation reaction of benzoyl radical: C<sub>6</sub>H<sub>5</sub>C(=O), *J. Phys. Chem. A*, 115, 11897-11914,  
1011 <https://doi.org/10.1021/jp2078067>, 2011.

1012 Shen, H., Vereecken, L., Kang, S., Pullinen, I., Fuchs, H., Zhao, D., and Mentel, T. F.: Unexpected  
1013 significance of a minor reaction pathway in daytime formation of biogenic highly oxygenated  
1014 organic compounds, *Sci. Adv.*, 8, eabp8702, <https://doi.org/10.1126/sciadv.abp8702>, 2022.

1015 Sun, J., Wu, F., Hu, B., Tang, G., Zhang, J., and Wang, Y.: VOC characteristics, emissions and  
1016 contributions to SOA formation during hazy episodes, *Atmos. Environ.*, 141, 560-570,  
1017 <https://doi.org/10.1016/j.atmosenv.2016.06.060>, 2016.

1018 Tajuelo, M., Bravo, I., Rodríguez, A., Aranda, A., Díaz-de-Mera, Y., and Rodríguez, D.:  
1019 Atmospheric sink of styrene,  $\alpha$ -methylstyrene, trans- $\beta$ -methylstyrene and indene: Rate  
1020 constants and mechanisms of Cl atom-initiated degradation, *Atmos. Environ.*, 200, 78-89,  
1021 <https://doi.org/10.1016/j.atmosenv.2018.11.059>, 2019c.

1022 Tajuelo, M., Rodríguez, A., Baeza-Romero, M. T., Aranda, A., Díaz-de-Mera, Y., and Rodríguez,  
1023 D.: Secondary organic aerosol formation from  $\alpha$ -methylstyrene atmospheric degradation:  
1024 Role of NO<sub>x</sub> level, relative humidity and inorganic seed aerosol, *Atmos. Res.*, 230,  
1025 104631-104640, <https://doi.org/10.1016/j.atmosres.2019.104631>, 2019b.

1026 Tajuelo, M., Rodríguez, D., Baeza-Romero, M. T., Díaz-de-Mera, Y., Aranda, A., and Rodríguez,  
1027 A.: Secondary organic aerosol formation from styrene photolysis and photooxidation with  
1028 hydroxyl radicals, *Chemosphere*, 231, 276-286,  
1029 <https://doi.org/10.1016/j.chemosphere.2019.05.136>, 2019a.

1030 Vereecken, L., Glowacki, D. R., and Pilling, M. J.: Theoretical chemical kinetics in tropospheric

1031 chemistry: methodologies and applications, *Chem. Rev.*, 115, 4063-4114,  
 1032 <https://doi.org/10.1021/cr500488p>, 2015.

1033 Wang, H., Ji, Y., Gao, Y., Li, G., and An, T.: Theoretical model on the formation possibility of  
 1034 secondary organic aerosol from OH initiated oxidation reaction of styrene in the presence of  
 1035 O<sub>2</sub>/NO, *Atmos. Environ.*, 101, 1-9, <https://doi.org/10.1016/j.atmosenv.2014.10.042>, 2015.

1036 Wang, L., Wu, R., and Xu, C.: Atmospheric oxidation mechanism of benzene. Fates of alkoxy  
 1037 radical intermediates and revised mechanism, *J. Phys. Chem. A*, 117, 14163-14168,  
 1038 <https://doi.org/10.1021/jp4101762>, 2013.

1039 Wang, M., Chen, D., Xiao, M., Ye, Q., Stolzenburg, D., Hofbauer, V., Ye, P., Vogel, A. L., Mauldin,  
 1040 R. L., Amorim, A., Baccharini, A., Baumgartner, B., Brilke, S., Dada, L., Dias, A., Duplissy, J.,  
 1041 Finkenzeller, H., Garmash, O., He, X. C., Hoyle, C. R., Kim, C., Kvashnin, A., Lehtipalo, K.,  
 1042 Fischer, L., Molteni, U., Petř T., Pospisilova, V., Quđ éver, L. L. J., Rissanen, M., Simon,  
 1043 M., Tauber, C., Tomé A., Wagner, A. C., Weitz, L., Volkamer, R., Winkler, P. M., Kirkby, J.,  
 1044 Worsnop, D. R., Kulmala, M., Baltensperger, U., Dommen, J., El-Haddad, I., and Donahue,  
 1045 N. M.: Photo-oxidation of aromatic hydrocarbons produces low-volatility organic compounds,  
 1046 *Environ. Sci. Technol.*, 54, 7911-7921, <https://doi.org/10.1021/acs.est.0c02100>, 2020.

1047 Wang, S., and Li, H.: NO<sub>3</sub>-initiated gas-phase formation of nitrated phenolic compounds in  
 1048 polluted atmosphere, *Environ. Sci. Technol.*, 55, 2899-2907,  
 1049 <https://doi.org/10.1021/acs.est.0c08041>, 2021.

1050 Wang, S., Newland, M. J., Deng, W., Rickard, A. R., Hamilton, J. F., Muñoz, A., Ródenas, M.,  
 1051 Vázquez, M. M., Wang, L., and Wang, X.: Aromatic photo-oxidation, a new source of  
 1052 atmospheric acidity, *Environ. Sci. Technol.*, 54, 7798-7806,  
 1053 <https://doi.org/10.1021/acs.est.0c00526>, 2020.

1054 Wang, S., Wu, R., Berndt, T., Ehn, M., and Wang, L.: Formation of highly oxidized radicals and  
 1055 multifunctional products from the atmospheric oxidation of alkylbenzene, *Environ. Sci.*  
 1056 *Technol.*, 51, 8442-8449, <https://doi.org/10.1021/acs.est.7b02374>, 2017.

1057 Wu, R., Pan, S., Li, Y., and Wang, L.: Atmospheric oxidation mechanism of toluene, *J. Phys.*  
 1058 *Chem. A*, 118, 4533-4547, <https://doi.org/10.1021/jp500077f>, 2014.

1059 Wu, X., Hou, Q., Huang, J., Chai, J., and Zhang, F.: Exploring the OH-initiated reactions of  
 1060 styrene in the atmosphere and the role of van der Waals complex, *Chemosphere*, 282,  
 1061 131004-131012, <https://doi.org/10.1016/j.chemosphere.2021.131004>, 2021.

1062 Wu, X., Huang, C., Niu, S., and Zhang, F.: New theoretical insights into the reaction kinetics of  
 1063 toluene and hydroxyl radicals, *Phys. Chem. Chem. Phys.*, 22, 22279-22288,  
 1064 <https://doi.org/10.1039/D0CP02984J>, 2020.

1065 Xu, C., and Wang, L.: Atmospheric oxidation mechanism of phenol initiated by OH radical, *J.*  
 1066 *Phys. Chem. A*, 117, 2358-2364, <https://doi.org/10.1021/jp308856b>, 2013.

1067 Xu, L., Møller, K. H., Crouse, J. D., Kjaergaard, H. G., and Wennberg, P. O.: New insights into  
 1068 the radical chemistry and product distribution in the OH-initiated oxidation of benzene,  
 1069 *Environ. Sci. Technol.*, 54, 13467-13477, <https://doi.org/10.1021/acs.est.0c04780>, 2020.

1070 Yan, Y., Cabrera-Perez, D., Lin, J., Pozzer, A., Hu, L., Millet, D. B., Porter, W. C., and Lelieveld,  
 1071 J.: Global tropospheric effects of aromatic chemistry with the SAPRC-11 mechanism  
 1072 implemented in GEOS-Chem version 9-02, *Geosci. Model Dev.*, 12, 111-130,  
 1073 <https://doi.org/10.5194/gmd-12-111-2019>, 2019.

1074 Yang, F., Deng, F., Pan, Y., Zhang, Y., Tang, C., and Huang, Z.: Kinetics of hydrogen abstraction

1075 and addition reactions of 3-hexene by OH radicals, *J. Phys. Chem. A*, 121, 1877-1889,  
1076 <https://doi.org/10.1021/acs.jpca.6b11499>, 2017.

1077 Yu, S., Jia, L., Xu, Y., and Pan, Y.: Formation of extremely low-volatility organic compounds from  
1078 styrene ozonolysis: Implication for nucleation, *Chemosphere*, 305, 135459-135467,  
1079 <https://doi.org/10.1016/j.chemosphere.2022.135459>, 2022.

1080 Yu, S., Jia, L., Xu, Y., and Pan, Y.: Molecular composition of secondary organic aerosol from  
1081 styrene under different NO<sub>x</sub> and humidity conditions, *Atmos. Res.*, 266, 105950-10604,  
1082 <https://doi.org/10.1016/j.atmosres.2021.105950>, 2022.

1083 Zaytsev, A., Koss, A. R., Breitenlechner, M., Krechmer, J. E., Nihill, K. J., Lim, C. Y., Rowe, J. C.,  
1084 Cox, J. L., Moss, J., Roscioli, J. R., Canagaratna, M. R., Worsnop, D. R., Kroll, J. H., and  
1085 Keutsch, F. N.: Mechanistic study of the formation of ring-retaining and ring-opening  
1086 products from the oxidation of aromatic compounds under urban atmospheric conditions,  
1087 *Atmos. Chem. Phys.*, 19, 15117-15129, <https://doi.org/10.5194/acp-19-15117-2019>, 2019.

1088 Zhang, H., Wang, J., Dong, B., Xu, F., Liu, H., Zhang, Q., Zong, W., and Shi, X.: New mechanism  
1089 for the participation of aromatic oxidation products in atmospheric nucleation, *Sci. Total  
1090 Environ.*, 917, 170487-170494, <https://doi.org/10.1016/j.scitotenv.2024.170487>, 2024.

1091 Zhang, R. M., Truhlar, D. G., and Xu, X.: Kinetics of the toluene reaction with OH radical,  
1092 *Research*, 2019, Article ID 5373785, <https://doi.org/10.34133/2019/5373785>, 2019.

1093 Zhao, H., Zhang, Y., Zhao, Q., Li, Y., and Huang, Z.: A theoretical study of H-abstractions of  
1094 benzaldehyde by H, O<sup>3</sup>(P), <sup>3</sup>O<sub>2</sub>, OH, HO<sub>2</sub>, and CH<sub>3</sub> radicals: Ab initio rate coefficients and  
1095 their uncertainty quantification, *J. Phys. Chem. A*, 126, 7523-7533,  
1096 <https://doi.org/10.1021/acs.jpca.2c02384>, 2022.

1097 Zhao, Y., and Truhlar, D. G.: The M06 suite of density functionals for main group  
1098 thermochemistry, thermochemical kinetics, noncovalent interactions, excited states, and  
1099 transition elements: two new functionals and systematic testing of four M06-class functionals  
1100 and 12 other functionals, *Theor. Chem. Acc.*, 120, 215-241,  
1101 <https://doi.org/10.1007/s00214-007-0310-x>, 2008.